CAPITAL UNIVERSITY OF SCIENCE AND TECHNOLOGY, ISLAMABAD

Attenuation from a Flexible Structure Backed by Porous Cavity

by

Usman Javeed

A thesis submitted in partial fulfillment for the degree of Master of Philosophy

in the

Faculty of Computing
Department of Mathematics

2025

I dedicate this endeavor to my beloved family, my cherished parents, my wife, inspiring teachers and my esteemed supervisor, Dr. Muhammad Afzal, who have been a constant source of motivation and guidance. Their unwavering support and countless contributions have been invaluable to me. I also extend this dedication to my precious child, who brings joy and purpose to my life every day. This achievement is a testament to their love, encouragement, and belief in me.

CERTIFICATE OF APPROVAL

Attenuation from a Flexible Structure Backed by Porous Cavity

by

Usman Javeed

(Registration No: MMT231013)

THESIS EXAMINING COMMITTEE

S. No.	Examiner	Name	Organization
(a)	External Examiner	Dr. Mahmood Ul Hassan	COMSATS, Islamabad
(b)	Internal Examiner	Dr. Muhammad Sabeel Khan	CUST, Islamabad
(c)	Supervisor	Dr. Muhammed Afzal	CUST, Islamabad

Dr.Muhammed Afzal
Thesis Supervisor
April, 2025

Dr. Muhammad Sagheer
Head
Dept. of Mathematics
April, 2025

Dr. M. Abdul Qadir
Dean
Faculty of Computing
April, 2025

Author's Declaration

I, **Usman Javeed** hereby state that my MS thesis titled "**Attenuation from a Flexible Structure Backed by Porous Cavity**" is my own work and has not been submitted previously by me for taking any degree from Capital University of Science and Technology, Islamabad or anywhere else in the country/abroad.

At any time if my statement is found to be incorrect even after my graduation, the University has the right to withdraw my MPhil Degree.

(Usman Javeed)

Registration No: MMT231013

Plagiarism Undertaking

I solemnly declare that research work presented in this thesis titled "**Attenuation from a Flexible Structure Backed by Porous Cavity**" is solely my research work with no significant contribution from any other person. Small contribution/help wherever taken has been duly acknowledged and that complete thesis has been written by me.

I understand the zero tolerance policy of the HEC and Capital University of Science and Technology towards plagiarism. Therefore, I as an author of the above titled thesis declare that no portion of my thesis has been plagiarized and any material used as reference is properly referred/cited.

I undertake that if I am found guilty of any formal plagiarism in the above titled thesis even after award of MS Degree, the University reserves the right to withdraw/revoke my MS degree and that HEC and the University have the right to publish my name on the HEC/University website on which names of students are placed who submitted plagiarized work.

(Usman Javeed)

Registration No: MMT231013

Acknowledgement

Words cannot fully express my heartfelt gratitude to Almighty Allah, the Most Merciful and Most Beneficent, whose endless blessings and grace have guided me through every step of this journey. I also extend my deepest appreciation to the last prophet of Allah, Prophet Hazrat Muhammad (S.A.W.), the greatest reformer and source of knowledge for humanity, whose teachings have illuminated the path of knowledge and wisdom.

I am sincerely grateful to everyone who supported and encouraged me throughout this journey. My special thanks go to my thesis supervisor, Dr. Muhammad Afzal, for his invaluable guidance and motivation. This thesis would have been incomplete without his dedicated efforts, which enabled me to complete it successfully.

I am profoundly grateful to my parents for their unwavering prayers, moral support, encouragement, and appreciation.

Lastly, but certainly not least, I would like to thank my friends and colleagues, whose support and assistance have been instrumental throughout my MPhil journey. Their companionship and encouragement have made this experience truly memorable.

(Usman Javeed)

Registration No: MMT231013

Abstract

This thesis investigates the acoustic attenuation properties of a flexible structure backed by a porous cavity, addressing three distinct boundary value problems. The interaction between acoustic waves and flexible structures plays a crucial role in noise reduction technologies, particularly in low-frequency sound absorption. The first problem examines the impedance condition for a flexible structure, analyzing how its inherent properties influence sound attenuation. The second problem explores the scenario where the flexible structure is backed by a rigid porous cavity, focusing on the interaction between the flexible structure and the rigid backing, and its impact on acoustic performance. The third problem considers the case of a flexible structure backed by a soft porous cavity, investigating the combined effects of flexibility and soft porous material on sound attenuation. Through theoretical modeling, numerical simulations, and experimental validation, this research provides a comprehensive understanding of the acoustic behavior in each configuration. The findings offer valuable insights for the design and optimization of noise control systems, particularly in applications where flexible structures and porous materials are employed to enhance acoustic performance. The results demonstrate that the choice of boundary conditions and cavity characteristics significantly influences the overall attenuation efficiency.

Contents

List of Figures

List of Tables

Abbreviations

BVPs	Boundary value problems
BCE	Before common era
MMT	Mode matching techniques
PDEs	Partial differential equations

Symbols

∇	Divergence
γ	Ratio of specific heat
ϕ	Fluid velocity potential
δ_{mn}	Kronecker delta
ρ	Instantaneous density
ω	Frequency
T	Tension
p_0	Equilibrium pressure
g	Gravitational acceleration
p	Instantaneous pressure
k	Wave number
Z_m^n	Average impedance of membrane for nth*mode*
c	Speed of sound
Z	Acoustic impedance
Z_{CF}	Impedance due to air-cavity and foam combination
Z_p	Panel impedance
$< u >_n$	Normal average velocity
α	Sound absorption coefficient
μ	Poisson's ratio

Chapter 1

Introduction

Noise often referred to as environmental noise or sound, is an increasingly pervasive issue in modern society. Defined as unwanted or excessive sound that disrupts the natural balance of life, noise is not only a nuisance but also a significant health hazard. From the constant hum of urban traffic to the roar of airplanes overhead, the sources of noise are diverse and widespread. Sound is a pressure wave that propagates through a medium (air, water, or solids), while vibration refers to the oscillatory motion of a mechanical system. Noise, on the other hand, is typically considered as an unwanted sound, often characterized by irregular or random vibrations. Noise, vibration, and sound are fundamental physical phenomena that play a critical role in various engineering and scientific disciplines. The earliest human interest in vibration likely stemmed from musical instruments such as whistles, drums, and stringed instruments.

Ancient Egyptians depicted harps on tomb walls as early as 3000 BCE, demonstrating an early understanding of sound production through vibrating strings. Pythagoras [1], a Greek mathematician, was one of the first to scientifically study vibrating strings using an instrument called the monochord. He discovered that the pitch of a note is related to the length of a vibrating string, forming the basis for later studies on acoustics. Aristotle [2] discussed sound in his works, describing it as a mechanical wave transmitted through a medium. Galileo Galilei [3] conducted pendulum experiments and recognized that the frequency of vibration is independent of amplitude for small oscillations. He studied vibrating strings and

laid the foundation for wave theory. Daniel Bernoulli [4] introduced the principle of superposition, which explains how multiple vibrations can coexist within a structure. Leonhard Euler and Jean d'Alembert [5, 6] derived the wave equation for vibrating strings, leading to mathematical models for sound propagation.

1.1 Causes of Noise :

1. **Urbanization:** The growth of cities and the concentration of human activities in urban areas have led to a surge in noise levels.

   Construction sites, industrial operations, and densely populated neighborhoods all contribute to the cacophony.

2. **Transportation:** Road traffic, railways, and air traffic are among the primary contributors to noise pollution.

   The constant movement of vehicles and the development of infrastructure to support them have exacerbated the problem.

3. **Industrial Activities:** Factories and manufacturing plants generate significant noise, often exposing workers and nearby residents to harmful levels of sound.

4. **Social Activities:** Events, parties, and public gatherings often involve loud music and amplifiers, adding to the ambient noise.

1.2 Effects of Noise:

Noise pollution has far-reaching consequences on both humans and the environment:

- **Health Issues:** Prolonged exposure to high noise levels can lead to hearing loss, stress, sleep disturbances, and cardiovascular problems. It can also impair concentration and productivity.

- **Impact on Wildlife:** Animals rely on sound for communication, navigation, and detecting predators. Excessive noise can disrupt these activities, leading to behavioral changes and reduced survival rates.

- **Reduced Quality of Life:** Constant exposure to noise diminishes the overall quality of life, creating a sense of annoyance and discomfort.

Addressing noise requires a combination of technological, regulatory, and behavioral approaches. As urbanization and industrialization continue to advance, addressing noise is becoming increasingly critical. By understanding its causes, recognizing its effects, and implementing effective strategies, society can work toward a quieter, healthier environment. Reducing noise is not only an investment in human well-being but also a step toward preserving the natural harmony of our world.

1.3 Background of the Study

Noise pollution is defined as the combination of sounds resulting to noise, thereby producing an annoying and disturbing sound. It is produced by different sources: aircraft noise, noise from railroads, construction noise, noise from vehicles, industrial noise and road trafic noise. Its effects are mainly affected by the duration and level of noise.

Ford and McCormick [7] developed the first theoretical model for square panel absorbers, incorporating the effects of plate bending waves and resonance behavior. They used the virtual work principle to derive the equation of motion for a thin, homogeneous, clamped plate subjected to plane wave excitation. Their model forms the foundation for later analyses of low-frequency sound absorption by vibrating panels.

Mode matching is a computational and analytical technique widely used in various fields such as electromagnetics, acoustics, optics, and quantum mechanics. It is particularly useful in dealing with problems involving discontinuities, waveguides, and multi-layered media, for instance see [8–18] . The primary goal of

mode matching is to ensure the continuity of fields (electric, magnetic, acoustic, etc.) across interfaces or boundaries between different regions or structures. This technique is particularly useful in solving boundary value problems where the solution must satisfy specific conditions at the boundaries. The core principle of the method is that the field in each region is expanded into a sum of eigen-modes that satisfy the boundary conditions of that region. The unknown coefficients of these modes are determined by enforcing continuity conditions at the interfaces between different regions. The origins of mode matching can be traced back to the early 20th century when researchers began to tackle complex boundary value problems in electromagnetics and acoustics. The technique gained significant traction with the advent of waveguide theory in the mid-20th century, where it was used to analyze and design microwave and optical waveguides. The mode matching technique relies on the following principles:

- Eigen-mode Expansion: The field in each sub-region of the problem is expanded using the appropriate basis functions (modes).
- Truncation: Since infinite series representations are impractical, the series is truncated to a finite number of terms to achieve an approximate but accurate solution.
- Continuity Conditions: The continuity of pressure, velocity, or electromagnetic fields is enforced at boundaries between regions.

The mode matching technique (MMT) is a powerful and versatile method for solving boundary value problems in various fields of science and engineering. By ensuring the continuity of fields across interfaces and leveraging the orthogonality of modes, it provides a systematic approach to analyzing and designing complex systems.

Despite its computational challenges, mode matching remains a fundamental tool in the arsenal of researchers and engineers dealing with wave propagation and field analysis, for instance [19–30] . MMT is commonly applied in acoustics, electromagnetics and structural vibrations. MMT help to analyze wave propagation in ducts, mufflers, and layered sound absorbers. MMT also helps in understanding

how vibration modes interact in complex geometries. MMT is particularly useful for panel sound absorbers, waveguides and ducts, perforated and microperforated panels. Some advantages of MMT are:

- Provides a precise and comprehensive approach to solve boundary value problems.
- Suitable for both analytical and numerical implementations.
- Works well in problems involving layered structures where boundary conditions can be explicitly formulated.
- Applicable to multiple domains like in electromagnetics, acoustics, and elasticity problems.

Few disadvatages of MMT are:

- MMT works best in problems with simple boundaries like rectangular or cylindrical structures; complex geometries require additional numerical techniques.
- Mode matching technique can become computationally intensive for problems with a large number of modes or complex geometries.
- Convergence issues may arise when dealing with highly irregular or discontinuous boundaries.

The Mode Matching Technique is a powerful tool for solving wave propagation problems, particularly in multi-region acoustic and electromagnetic systems. It is highly effective for systems involving layered media and discontinuities, making it useful for sound absorbers, waveguides, and resonators.

Fuchs [31] investigated the sound absorption characteristics of panel systems, focusing on the effects of surface mass of the panel and thickness of the air cavity. Fuchs concluded that increasing the mass and cavity thickness shifts the absorption peak to lower frequencies, but space and cost constraints limit these changes. He highlighted the trade-off between practical design and acoustic performance.

A porous medium consists of a solid matrix with interconnected void spaces or pores, allowing the passage of fluids or sound waves. These materials are widely used in acoustics, filtration, insulation, and various engineering applications. Their unique properties arise from the interaction between the fluid (air, water, or other substances) and the solid framework. The study of porous media dates back to ancient civilizations, where the principles of fluid flow through porous materials were intuitively understood and applied. However, the formal scientific investigation of porous media began in the 19th century with the development of groundwater hydrology and petroleum engineering.

Ancient civilizations, such as the Romans and Greeks, used porous materials like sand and gravel for water filtration and storage. The concept of water flow through soil and rocks was observed and utilized in early agricultural practices. The foundational work in the field of porous media was conducted by Henry Darcy [32], a French engineer. He formulated Darcy's Law, which describes the flow of a fluid through a porous medium. In 20th Century M. King Hubbert [33] extended Darcy's work to include the flow of oil and gas in petroleum reservoirs, leading to the development of reservoir engineering. Philip and de Vries [34] developed models for water and heat transport in unsaturated soils, which are crucial for agricultural and environmental applications. Bear and Bachmat [35] contributed significantly to the theoretical understanding of transport phenomena in porous media, including the development of the concept of effective properties and the use of volume averaging techniques. Modern Era advances in computational methods and experimental techniques have allowed for more detailed and accurate modeling of fluid flow and transport in porous media. Porous media have a wide range of applications, including Hydrology, Petroleum Engineering, Environmental Science, Chemical Engineering and Materials Science. Models such as Biot's theory and the Delany-Bazley model describe wave propagation in porous media. These models account for factors like pore structure, fluid interaction, and boundary constraints, essential for designing effective sound absorbers. Porous media are essential in noise control applications, particularly for low-frequency absorption. Understanding their physical properties and behavior in different configurations allows for optimizing architectural acoustics, automotive soundproofing, and industrial noise reduction. The research article applies these principles to circular

panel absorbers, demonstrating the effectiveness of air cavities and porous materials in controlling sound.

Fasold and Veres [36] suggested that the thickness of the air cavity should be optimized to avoid being too small (reducing absorption) or too large (inefficient use of space). Wang et al. [37] applied vibrating plates for noise control by attaching clamped plates with air cavities to the walls of ducts. He demonstrated that non-homogeneous plates achieved better sound absorption compared to homogeneous plates. Frommhold et al. [38] investigated thin vibrating plates on honeycomb structures, where the enclosed air acted as a Helmholtz resonator. He found that such systems exhibited two resonances, one due to the Helmholtz resonator and another due to the plate's stiffness.

Lee et al. [39] conducted both theoretical and experimental studies on micro-perforated panels (MPPs) backed by air cavities. He showed that micro-perforations introduced acoustic resistance, improving mid-frequency absorption while slightly compromising low-frequency performance. He noticed the presence of dual peaks in absorption, one due to the panel resonance and another due to the Helmholtz resonance of the cavity.

Tayong et al. [40] explored the nonlinear behavior of MPP systems at high sound pressure levels. He demonstrated that the absorption peak depended on the flow velocity through the micro-perforations. Sakagami et al. [41] analyzed the vibration and acoustic behavior of infinite elastic panels and MPPs. He showed that structural vibrations degraded sound absorption at low frequencies but improved it at higher frequencies. Hiraizumi et al. [42] analyzed the sound absorption of circular panels with clamped boundaries. Their work focused on solving the wave equation in cylindrical coordinates, without using electrical analogies. They did not consider elastic boundary conditions, which limited the generalizability of their model. The application of a vibrating plate to absorb low-frequency noise was presented by Wang et al. [37]. They employed this physical principle to add a completely clamped plate with a sealed air-back cavity to the sidewall of a duct to reduce the transmitted sound. The analysis was developed for homogeneous and nonhomogeneous plates; better sound-absorption values were obtained for the latter.

The case of an infinite elastic panel with an air-back cavity has been analyzed by Sakagami et al. [43, 44] for an arbitrary angle of incidence. Their results indicated that the contribution of the air cavity is dominant and that the contribution to the sound absorption of the panel's damping loss factor is negligible. Obviously, the effect of structural resonance of the panel was not included because this effect appears only when the panel is finite and reflections occur at the boundaries. Subsequently, Sakagami et al. [41] included the effect of the vibration of the micro-perforated panel in a simplified manner, considering the surface density of the plate for inclusion into the impedance equations of the equivalent circuit. Thus, the reactance of the panel's mass was added in parallel to the impedance of the micro-perforations. The results showed that a very light panel reduced the amplitude of the absorption peak and slightly increased the resonance frequency. However, for panels having a surface mass greater than $2kg/m^2$, the difference was very small and the maximum value of absorption was almost the same as in the case of a immobile panel. Lee and Swenson [39, 45] analyzed low-frequency sound absorbers both theoretically and experimentally using one or two square perforated panels with an air-back cavity. During the experimental work they noticed the presence of absorption peaks at very low frequencies that were associated with the panel vibration. In the work of Frommhold et al. [38] , a thin vibrating panel on a light honeycomb structure was studied. This system formed small air volumes, which acted as Helmholtz resonators. They used the expression of Ford and McCormick [46] to include the effect of mechanical vibration of the plate in the theoretical model to estimate the sound absorption of the system. It was concluded that the system had two resonances, one associated with the Helmholtz resonator and the other with the stiffness of the plate.

Many earlier works assumed perfect clamping conditions for the plate boundaries. However, achieving perfect clamping is challenging in practice, and real systems often have elastic boundary conditions. The mode matching method is found usefull to address boundary value problems involving different edge conditions for instance [47–59]. The current study extends the work by incorporating fixed boundary conditions into the theoretical model. Deriving a expression for sound absorption that accounts for flexural vibrations of the membrane, fixed boundary conditions, and the effects of air and porous materials.

Chapter 2

Preliminaries

This chapter contains fundamental definitions and governing principles related to waves and acoustics.

2.1 Wave

A wave is a disturbance or oscillation that travels through space and matter, transferring energy from one point to another without transporting matter. Examples include:

- **Mechanical Waves** (e.g., sound waves, water waves) that require a medium like air, water, or solid to propagate.

- **Electromagnetic Waves** (e.g., light waves, radio waves) that can propagate through a vacuum.

Categories of waves are: Transverse waves (where the oscillation is perpendicular to the wave direction, e.g., light waves) and Longitudinal waves (where the oscillation is parallel to the wave direction, e.g., sound waves).

2.2 Acoustics

The word acoustics has its origins in the ancient Greek language and has evolved over centuries to its current usage. The word "acoustics" derives from the Greek word akoustikos meaning "pertaining to hearing". This, in turn, comes from akouein, which means "to hear".

The ancient Greeks were among the first to study sound scientifically. Philosophers like Pythagoras, Aristotle, and later, Vitruvius in Rome, explored the principles of sound, including its propagation and its relationship with music and architecture. Acoustics is the branch of science concerned with the study of sound, its production, transmission, and effects. It encompasses a wide range of topics and applications, including the behavior of sound waves in various environments, the design of spaces to optimize sound, and the development of technologies for sound recording and reproduction.

2.3 Acoustic Wave

An acoustic wave is a type of mechanical wave that propagates through a medium (such as air, water, or a solid) as a result of oscillations in pressure, density, and particle displacement. These waves transfer energy from one point to another without transporting matter.

2.4 Acoustic Wave Equation

The acoustic wave equation can be derived from the fundamental principles of fluid mechanics, including the conservation of mass, conservation of momentum, and the equation of state for a fluid. Here's a detailed derivation:

1. **Conservation of Mass (Continuity Equation)** The continuity equation for a compressible fluid is given by:

$$\frac{\partial \rho}{\partial t} + \nabla.(\rho v) = 0. \tag{2.1}$$

Substituting $\rho = \rho_0 + \rho^*$ into (2.1), we get

$$\frac{\partial}{\partial t}(\rho_0 + \rho^*) + \nabla.[(\rho_0 + \rho^*)v] = 0. \tag{2.2}$$

Since ρ_0 is a constant (steady background density), its time derivative vanishes, so from (2.2) we get

$$\frac{\partial \rho^*}{\partial t} + \nabla.[(\rho_0 + \rho^*)v] = 0. \tag{2.3}$$

To linearize, we assume that the perturbation ρ^* is small, meaning products of small perturbations $(\rho^* v)$ are negligible, by neglecting $\nabla.(\rho^* v)$ in (2.3), we get the continuity equation

$$\frac{\partial \rho^*}{\partial t} + \rho_0 \nabla.v = 0. \tag{2.4}$$

2. **Conservation of Momentum** The Navier-Stokes equation for a compressible, inviscid fluid is:

$$\rho \left(\frac{\partial v}{\partial t} + (v.\nabla)v \right) = -\nabla p. \tag{2.5}$$

By using same substitution as we used in conservation of mass and linearizing in same way we get

$$\rho_0 \frac{\partial v}{\partial t} = -\nabla p^*. \tag{2.6}$$

3. **Equation of State** For a compressible fluid, the equation of state relates pressure and density.

$$p^* = c^2 \rho^*. \tag{2.7}$$

4. **Combine the Equations** From the continuity equation (2.4), we get

$$\nabla.v = -\frac{1}{\rho_0} \frac{\partial \rho^*}{\partial t}. \tag{2.8}$$

From the momentum equation (2.6), we get

$$\frac{\partial v}{\partial t} = -\frac{\nabla p^*}{\rho_0}. \tag{2.9}$$

By using (2.7) into (2.9), we get

$$\frac{\partial v}{\partial t} = -\frac{\nabla(c^2\rho^*)}{\rho_0} = -c^2\frac{\nabla\rho^*}{\rho_0}.$$

On taking divergence of both sides, we get

$$\nabla.\frac{\partial v}{\partial t} = -c^2\nabla.\frac{\nabla\rho^*}{\rho_0}. \tag{2.10}$$

From the continuity equation,

$$\nabla.\frac{\partial v}{\partial t} = -\frac{\partial}{\partial t}\left(\frac{1}{\rho_0}\frac{\partial\rho^*}{\partial t}\right). \tag{2.11}$$

Thus

$$-\frac{\partial}{\partial t}\left(\frac{1}{\rho_0}\frac{\partial\rho^*}{\partial t}\right) = -c^2\nabla.\frac{\nabla\rho^*}{\rho_0}. \tag{2.12}$$

On simplifying

$$\frac{\partial^2\rho^*}{\partial t} = c^2\nabla^2\rho^*, \tag{2.13}$$

which is the acoustic wave equation for air, describing the propagation of density fluctuations.

On substituting $p^* = c^2\rho^*$, the wave equation can also be written for pressure fluctuations as:

$$\frac{\partial^2 p^*}{\partial t} = c^2\nabla^2 p^*. \tag{2.14}$$

2.5 Boundary Conditions

When solving partial differential equations (PDEs) like the acoustic wave equation, boundary conditions (BCs) are necessary to ensure the solution is well-defined.

These conditions specify the behavior of the solution at the boundaries of the domain.

2.5.1 Dirichlet Boundary Conditions (Fixed Value)

These boundary conditions specify the value of the variable (e.g., pressure or displacement) on the boundary.

$$u(x,t) = g(x,t).$$

Example: The pressure p at the boundary of a cavity is held constant ($p = 0$ or any specified function). In physical context, fixed temperature in heat conduction, fixed displacement in structural mechanics, or constant pressure in acoustics.

2.5.2 Neumann Boundary Conditions (Flux or Gradient)

These boundary conditions specify the derivative (gradient or flux) of the variable normal to the boundary.

$$\frac{\partial u}{\partial t} = h(x,t).$$

Example: The rate of change of pressure or velocity is specified at the boundary. In physical context, Heat flux in thermal problems or particle flux in diffusion problems.

2.5.3 Robin Boundary Conditions (Mixed Type)

A linear combination of Dirichlet and Neumann conditions:

$$au + b\frac{\partial u}{\partial t} = f(x,t),$$

where a, b, and f are given coefficients.

Example: Robin boundary conditions describe partially reflective boundaries where energy is both transmitted and reflected. In physical context, convection and radiation problems in heat transfer, or partially absorbing acoustic boundaries.

2.6 Impedance Translation Theorem

The impedance translation theorem states that the impedance at one point along a transmission line (or waveguide) can be transformed to another point along the same line, taking into account the propagation characteristics of the medium. This theorem is essential for analyzing wave propagation, impedance matching, and energy reflection in systems involving layers such as air cavities and porous materials.

Chapter 3

Impedance Conditions For Flexible Structure

In this chapter, we examine acoustic propagation and scattering along a membrane interface. The governing boundary value problems (BVPs) involve the Helmholtz equation, rigid conditions, membrane conditions, and edge conditions. The eigenfunctions in the specified duct regions exhibit orthogonality. By applying matching conditions and leveraging well-defined orthogonal properties, the problem is effectively solved. A detailed discussion of this process is presented in this chapter sectionwise.

3.1 Mathematical Formulation

Figure 3.1 represents the physical model of a low-frequency sound absorber made of a circular panel with an elastic boundary condition. The panel is a thin, circular membrane of radius a and thickness h , excited by a plane sound wave of constant amplitude. The panel vibrates in response to the incident sound, inducing flexural oscillations. Directly below the circular panel, there is an air cavity with thickness d_1. This acts as a spring that contributes to the system's overall acoustic impedance. Below the air cavity is a layer of porous sound-absorbing material with thickness d_2. This material dissipates sound energy, improving the absorption characteristics of the system. At the bottom of the assembly is a rigid

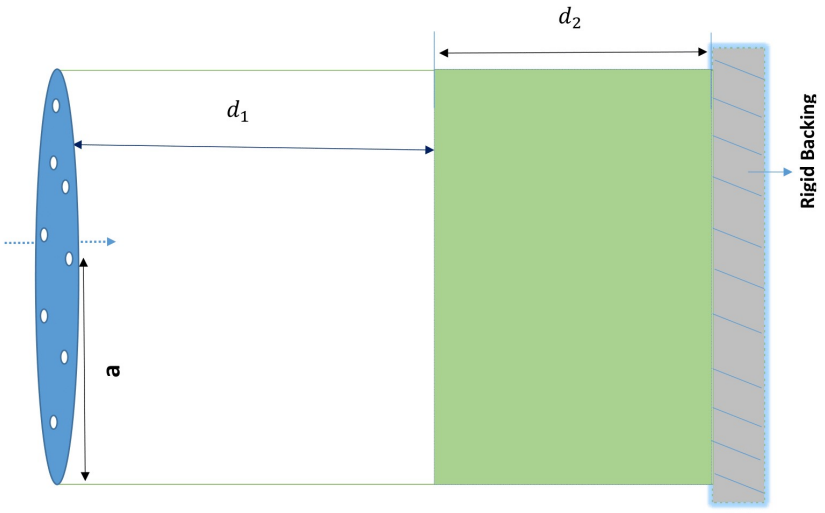

FIGURE 3.1: The circular panel absorber.

surface with ideal infinite acoustic impedance, ensuring no sound energy through it. The incident sound wave induces vibrations in the plate, which then propagate through the air cavity and the porous material, eventually being reflected and absorbed by the system.

The low-frequency sound absorber is represented in Figure 3.1. A plane sound wave of amplitude ρ_0 coming from the left strikes an impervious layer formed by a thin plate with radius a and thickness h. This sound wave induces a vibration that is propagated through the air cavity of thickness d_1 and through a sound absorbing layer of thickness d_2, which is resting in front of a rigid backing surface with ideal infinite acoustic impedance.

3.2 Mode Matching Solution:

The motion of a membrane or plate typically arises from the fundamental principles of elasticity and vibration theory. These systems are commonly modeled using partial differential equations (PDEs) that describe the displacement or deflection of the membrane/plate under the influence of external forces or boundary conditions. Membranes are thin, flexible structures where bending is ignored, and the displacement occurs due to in-plane tension forces. The governing equation is second-order and reflects the balance of in-plane forces. Plates are thicker and

can experience both bending and stretching. The governing equation is of fourth order and accounts for both bending resistance and in-plane forces.

The plate equation accounts for flexural rigidity and is often used to model structures like beams, slabs, and thin plates under load. Both equations are fundamental in understanding the behavior of thin structures under various loading conditions, with the membrane equation being simpler and used in situations where bending effects are negligible, and the plate equation accounting for both bending and stretching. The equation of membrane vibration is:

$$T\nabla^2 W + 2i\omega\eta\nabla^2 W + \omega^2\rho_p W = f(r), \tag{3.1}$$

where T represent stiffness constant or more specifically the tension per unit length in the membrane, ω is the angular frequency of waves, η is a damping coefficient, representing some form of energy dissipation, ρ_p is the density (or mass density) of the medium through which the wave propagates, W is the unknown function that depends on spatial variables and ∇^2 is the Laplacian operator, which represents the sum of second spatial derivatives of a function.

By putting $k_p^2 = \omega^2\rho_p/D$, $D = T + 2i\omega\eta$, $F(r) = f(r)/D$, (3.1) takes the form

$$(\nabla^2 + k_P^2)W(r) = F(r). \tag{3.2}$$

We assume the solution of (3.2) as

$$W(r) = \sum_{n=0}^{\infty} \gamma_n \phi_n(r), \tag{3.3}$$

where $\phi_n(r)$ satisfy the eigenvalue problem associated with (3.2) and can be expressed as

$$(\nabla^2 + k_n^2)\phi_n = 0. \tag{3.4}$$

In cylindrical coordinates, the governing equations for systems are typically written in terms of the radial coordinate r and the angular coordinate θ as:

$$\nabla^2 = \frac{\partial^2}{\partial r^2} + \frac{1}{r}\frac{\partial}{\partial r} + \frac{1}{r^2}\frac{\partial^2}{\partial \theta^2}.$$

For axisymmetric modes, the displacement does not depend on θ, so the problem simplifies to one variable r as,

$$\nabla^2 = \frac{\partial^2}{\partial r^2} + \frac{1}{r}\frac{\partial}{\partial r}. \tag{3.5}$$

Upon substituting (3.5) into (3.4), we have

$$\frac{\partial^2 \phi_n}{\partial r^2} + \frac{1}{r}\frac{\partial \phi_n}{\partial r} + k_n^2 \phi_n = 0, \tag{3.6}$$

with boundary condition

$$\phi_n(a) = 0. \tag{3.7}$$

By solving (3.6), we get

$$\phi_n(r) = AJ_0(k_n r) + BN_0(k_n r), \tag{3.8}$$

where J_0 and N_0 are modified Bessel's functions of first and second kind respecively, when $r \to 0$, then $N_0 \to \infty$. We assume $B = 0$ for defined solution in given domain, therefore

$$\phi_n(r) = AJ_0(k_n r). \tag{3.9}$$

Using (3.7) into (3.9), we have

$$0 = AJ_0(k_n a),$$

or

$$J_0(k_n a) = 0. \tag{3.10}$$

To prove the orthogonality relation, consider two eigenfunctions $\phi_m(r)$ and $\phi_n(r)$ corresponding to distinct eigenvalues k_m^2 and k_n^2 respectively.

We can rewrite (3.6) in the standard form of a Sturm-Liouville problem as

$$\frac{d}{dr}\left(r\frac{d\phi_n(r)}{dr}\right) = -k_n^2 r\phi_n(r), \tag{3.11}$$

and

$$\frac{d}{dr}\left(r\frac{d\phi_m(r)}{dr}\right) = -k_m^2 r\phi_m(r). \tag{3.12}$$

Multiplying equation (3.12) by $\phi_n(r)$, we get

$$\phi_n(r)\left[\frac{d}{dr}\left(r\frac{d\phi_m(r)}{dr}\right)\right] = -k_m^2 r\phi_m(r)\phi_n(r). \tag{3.13}$$

Multiplying equation (3.11) by $\phi_m(r)$,

$$\phi_m(r)\left[\frac{d}{dr}\left(r\frac{d\phi_n(r)}{dr}\right)\right] = -k_n^2 r\phi_m(r)\phi_n(r). \tag{3.14}$$

Subtracting (3.13) and (3.12), we get

$$\phi_n(r)\left[\frac{d}{dr}\left(r\frac{d\phi_m(r)}{dr}\right)\right] - \phi_m(r)\left[\frac{d}{dr}\left(r\frac{d\phi_n(r)}{dr}\right)\right] = (k_n^2 - k_m^2) r\phi_m(r)\phi_n(r). \tag{3.15}$$

Integrating (3.15) both sides from 0 to a, we have

$$\int_0^a \left[\phi_n(r)\frac{d}{dr}\left(r\frac{d\phi_m(r)}{dr}\right) - \phi_m(r)\frac{d}{dr}\left(r\frac{d\phi_n(r)}{dr}\right)\right] dr = (k_n^2 - k_m^2)\int_0^a r\phi_m(r)\phi_n(r)\, dr. \tag{3.16}$$

The left-hand side of (3.16) can be simplified using integration by parts. After applying the boundary condition $\phi_m(a) = \phi_n(a) = 0$, the left-hand side turns to be zero and we get

$$0 = (k_n^2 - k_m^2) \int_0^a r\phi_m(r)\phi_n(r)\, dr. \tag{3.17}$$

If $k_n^2 - k_m^2 \neq 0$, then (3.17) becomes

$$\int_0^a r\phi_m(r)\phi_n(r)dr = 0. \tag{3.18}$$

If $k_n^2 - k_m^2 = 0$, then (3.17) becomes

$$\int_0^a r\phi_m(r)\phi_n(r)dr = \chi_n\delta_{mn}, \tag{3.19}$$

where

$$\chi_n = \int_0^a \phi_n^2 r dr. \tag{3.20}$$

So we have

$$\int_0^a r\phi_m(r)\phi_n(r)\, dr = 0, \quad \text{for } m \neq n.$$

The orthogonality relation is

$$\int_0^a r\phi_m(r)\phi_n(r)dr = \chi_n\delta_{mn}, \tag{3.21}$$

Equation (3.10) is a dispersion relation and gives non-trivial solution. The function $\{\phi_n(r), n = 0, 1, 2, ...\}$ are orthogonal and satisfy the orthogonality relation (3.21).

By substituting (3.3) into (3.2), we get

$$\sum_{n=0}^{\infty} \gamma_n (\nabla^2 + k_p^2)\phi_n = F(r).$$

Using (3.5), we have

$$\sum_{n=0}^{\infty} \gamma_n \Big[\Big(\frac{\partial^2 \phi_n}{\partial r^2} + \frac{1}{r} \frac{\partial \phi_n}{\partial r} \Big) + k_p^2 \phi_n \Big] = F(r). \tag{3.22}$$

From (3.6), we have

$$\frac{\partial^2 \phi_n}{\partial r^2} + \frac{1}{r} \frac{\partial \phi_n}{\partial r} = -k_n^2 \phi_n. \tag{3.23}$$

Upon using (3.23) into (3.22), we get

$$\sum_{n=0}^{\infty} \gamma_n (k_p^2 - k_n^2)\phi_n = F(r). \tag{3.24}$$

On multiplying (3.24) with $r\phi_m$, we have

$$\sum_{n=0}^{\infty} \gamma_n (k_p^2 - k_n^2)\phi_n \phi_m r = F(r) r \phi_m. \tag{3.25}$$

Integrating (3.25) from 0 to a, we get

$$\sum_{n=0}^{\infty} \gamma_n (k_p^2 - k_n^2) \int_0^a \phi_n \phi_m r dr = \int_0^a F(r) r \phi_m dr. \tag{3.26}$$

On using orthogonality relation (3.21), equation (3.26) yields

$$\sum_{n=0}^{\infty} \gamma_n \Delta_n \delta_{mn} \chi_n = \int_0^a F(r) \phi_m r dr, \tag{3.27}$$

or

$$\gamma_m \Delta_m \chi_m = \int_0^a F(r) \phi_m r dr,$$

or

$$\gamma_m = \frac{1}{\Delta_m \chi_m} \int_0^a F(r)\phi_m r dr, \tag{3.28}$$

where

$$\Delta_m = k_p^2 - k_n^2. \tag{3.29}$$

Replacing m with n into (3.28), we get

$$\gamma_n = \frac{1}{\Delta_n \chi_n} \int_0^a F(r)\phi_n r dr. \tag{3.30}$$

Using (3.30) into (3.3), the resulting displacement is

$$W(r) = \sum_{n=0}^{\infty} \frac{\phi_n(r)}{\Delta_n \chi_n} \int_0^a F(\tau)\phi_n(\tau)\tau d\tau. \tag{3.31}$$

If we assume $F(\tau) = f(r)/D$ and also consider that the distributed force per unit area is constant sound pressure p_0, (3.31) becomes

$$W(r) = \frac{p_0}{D} \sum_{n=0}^{\infty} \frac{\phi_n(r)}{\Delta_n \chi_n} \int_0^a \phi_n(\tau)\tau d\tau. \tag{3.32}$$

Ford and McCormick [46] developed a theoretical framework for calculating the motion and acoustic response of vibrating plates under clamped boundary conditions, particularly for sound absorbers. Their model uses the virtual work principle to derive equations describing the modal behavior of a plate.

Lee and collaborators [39] extended the analysis to include various configurations like microperforated plates with Helmholtz resonances and additional effects like air-cavity interactions. They emphasized the role of the modal properties of the plate in determining sound absorption characteristics. The definition given by Ford and McCormick [46] and Lee et al. [39] is

$$< W >_n = \frac{1}{s} \int \int_s W_n(r) ds. \tag{3.33}$$

Equation (3.33) aligns with their methodology by defining the spatial-average displacement amplitude of the circular membrane under axisymmetric vibrations. It extends their principle to circular membrane with elastic boundary conditions. Lee et al. incorporate these considerations by coupling the modal analysis of the plate's vibration (as influenced by its boundary conditions) with the acoustic impedance effects of the air cavity. As $s = \pi a^2$, (3.33) becomes

$$< W >_n = \frac{1}{\pi a^2} \int_0^{2\pi} \int_0^a W_n(r) dr d\theta,$$

or

$$< W >_n = \frac{2}{a^2} \int_0^a W_n(r) r dr, \tag{3.34}$$

where

$$W_n(r) = \frac{p_0 \phi_n(r)}{D \Delta_n \chi_n} \int_0^a \phi_n(\tau) \tau d\tau. \tag{3.35}$$

Using (3.35) into (3.34), we get

$$< W >_n = \frac{2p_0}{Da^2 \Delta_n \chi_n} \Big[\int_0^a \phi_n(r) r dr \Big]^2. \tag{3.36}$$

Thus the average displacement is

$$< W > = \sum_{n=0}^{\infty} < W >_n . \tag{3.37}$$

Using (3.36) into (3.37), we get

$$< W > = \sum_{n=0}^{\infty} \frac{2p_0}{Da^2 \Delta_n \chi_n} \Big[\int_0^a \phi_n(r) r dr \Big]^2. \tag{3.38}$$

The average impedance of n^{th} mode is

$$Z_m^n = \frac{p}{< u >_n}. \tag{3.39}$$

Using $p = p_0$, equation (3.39) becomes

$$Z_m^n = \frac{p_0}{< u >_n}. \tag{3.40}$$

In (3.40), $< u >_n$ represents the normal average velocity and is given by

$$< u >_n = i\omega < W >_n . \tag{3.41}$$

By using (3.36) into (3.41), we get

$$< u >_n = i\omega \frac{2p_0}{Da^2 \Delta_n \chi_n} \Big[\int_0^a \phi_n(r) r dr \Big]^2. \tag{3.42}$$

Upon substituting (3.42) into (3.40), we have

$$Z_m^n = \frac{p_0}{i\omega \frac{2p_0}{Da^2 \Delta_n \chi_n} \Big[\int_0^a \phi_n(r) r dr \Big]^2}.$$

By simplifying, we get

$$Z_m^n = \frac{Da^2 \Delta_n \chi_n}{2i\omega \Big[\int_0^a \phi_n(r) r dr \Big]^2}. \tag{3.43}$$

The total impedance of the absorber can be expressed as the sum of the membrane's impedance and the combined impedance of the cavity and porous material. Mathematically,

$$Z = Z_m + Z_{CF}. \tag{3.44}$$

The membrane impedance Z_m is derived from the motion of the circular membrane under the influence of an external pressure wave. Mathematically, Z_m is represented as a combination of real and imaginary parts, as derived in (3.31)

$$Z_m^{-1} = \sum (Z_m^n)^{-1}, \tag{3.45}$$

where Z_m^n is the specific acoustic impedance of the membrane at the n^{th} mode.

By applying the impedance translation theorem, where the effective impedance combines the contributions from the cavity and foam layers.

Z_{CF} represents the impedance due to the air cavity and porous material behind the plate, which influences how sound waves interact with the absorber. It is given by

$$Z_{CF} = \frac{Z_0^2 + Z_1 Z_2}{Z_1 + Z_2}, \tag{3.46}$$

where $Z_0 = \rho_0 c$ (characteristic impedance of the air),

$Z_1 = -iZ_0 \cot(kd_1)$ (the acoustic impedance of the air cavity), as Z_1 gives the acoustic impedance of the air cavity, which acts as a spring in the system and the term $\cot(kd_1)$ introduces frequency-dependent behavior, creating resonance conditions for specific cavity thicknesses and frequencies. The acoustic impedance of the porous layer is $Z_2 = -iZ_C \cot(\Gamma d_2)$ where Z_C is the characteristic impedance of the foam and Γ is the propagation constant of the foam. Note that Γ and Z_C can be determined either experimentally or by using a specific model. As Z_2 is the acoustic impedance of the porous layer, which dissipates energy and contributes to sound absorption.

3.2.1 Graphical Results of Impedance Condition For Flexible Structure

This section presents a systematic investigation of the graphical results characterizing the impedance condition at the membrane interface. We analyze the acoustic

wave propagation dynamics and scattering phenomena generated by the interaction of incident sound waves with the membrane structure. To achieve computational precision, the series solution is truncated to the first 10 terms, ensuring a balance between numerical efficiency and physical accuracy. Through parametric studies, we quantify the dependence of the effective impedance on three critical variables, first one is frequency of the incident acoustic field, second is tension applied to the membrane, and third is radius of the membrane.

These relationships are visualized using comparative plots, revealing trends such as impedance amplification at resonant frequencies and attenuation under increased tension. The results provide actionable insights for optimizing membrane-based acoustic metamaterials in noise control and wave manipulation applications.

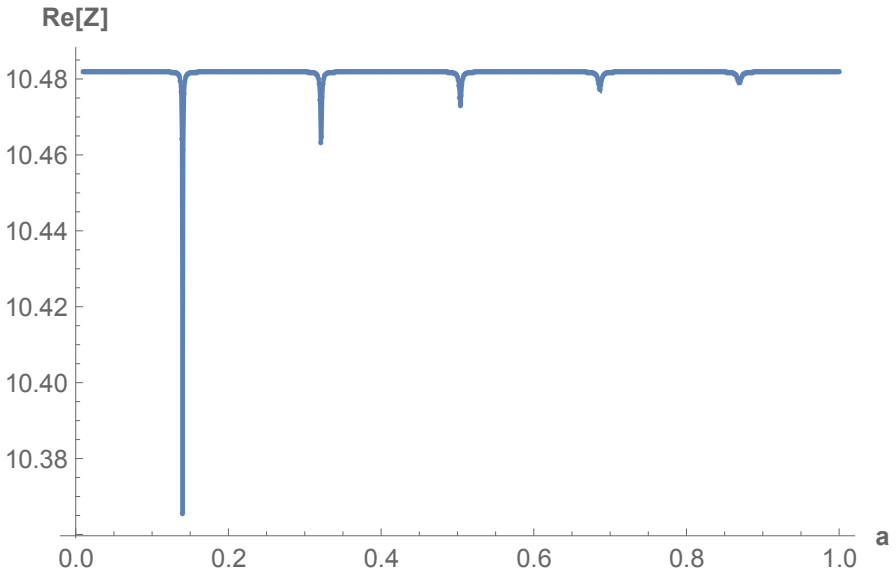

FIGURE 3.2: Graph of real part of Z against radius a.

Figure 3.2 represents the variation of the real part of impedance ($Re[Z]$) as a function of radius a. The x-axis represents the values of a ranging from 0 to 1.0, while the y-axis shows the corresponding $Re[Z]$ values. The low impedance at $a = 0.14$ indicates that more energy is being absorbed.

Figure 3.3 depicts the variation of the imaginary part of impedance ($Im[Z]$) as a function of radius a. The x-axis represents the values of a ranging from 0 to 1.0, while the y-axis shows the corresponding $Im[Z]$ values. The graph indicates a resonance frequency, which signifies efficient energy transmission.

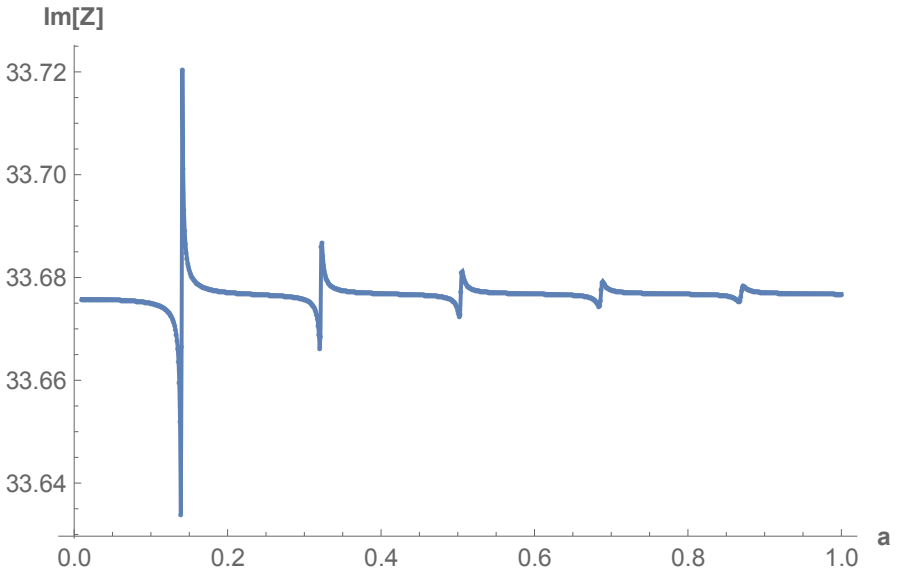

FIGURE 3.3: Graph of imaginary part of Z against radius a.

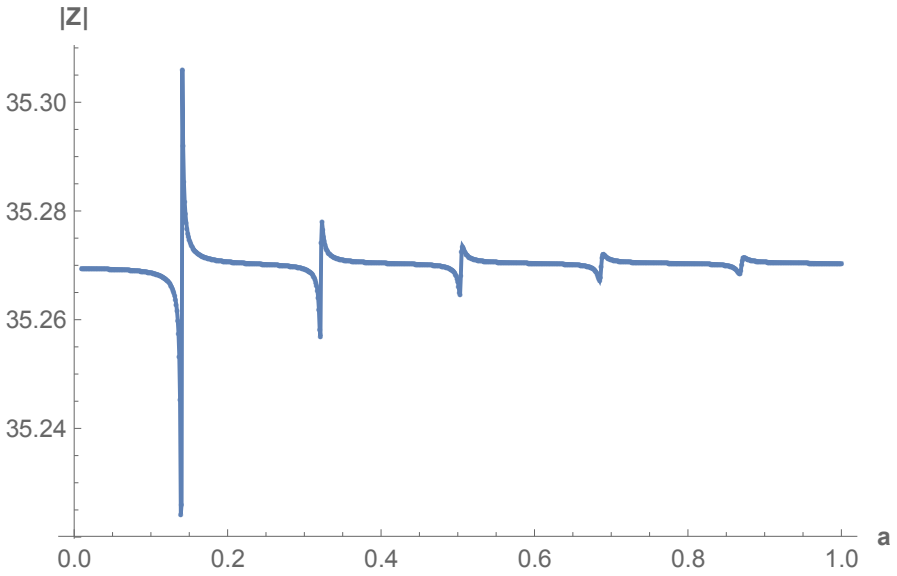

FIGURE 3.4: Graph of absolute part of Z against radius a.

Figure 3.4 illustrates the variation of the absolute part of impedance Z as a function of radius a. The x-axis represents the values of a ranging from 0 to 1.0, while the y-axis shows the corresponding absolute values of Z . The graph indicates overall behavior of impedance. Figure 3.5 shows the variation of the real part of impedance Z as a function of tension T. The x-axis represents tension values ranging from 0 to 1000, while the y-axis shows the corresponding real values, which decrease significantly from 250 to 50. At $T = 500$, impedance is high, indicating that more energy is reflected rather than absorbed.

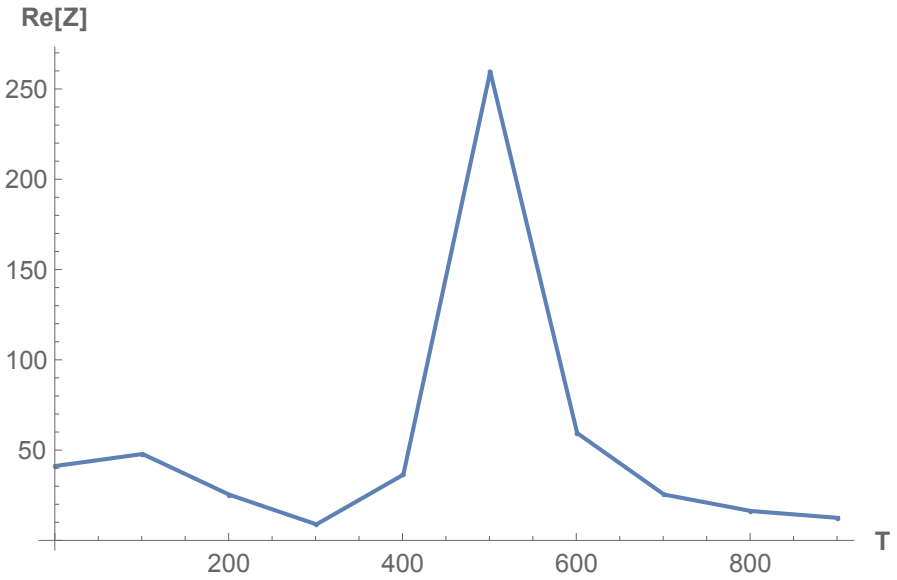

FIGURE 3.5: Graph of real part of Z against tension T.

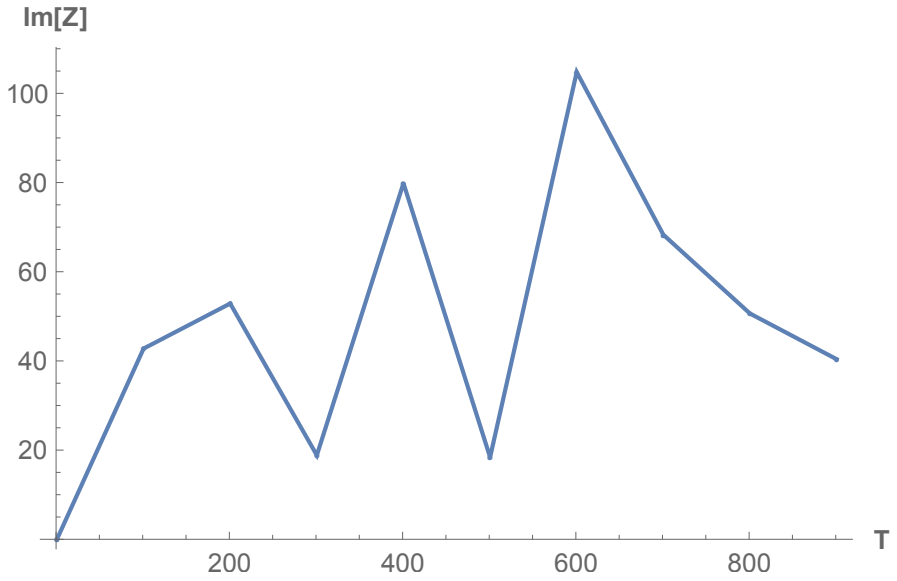

FIGURE 3.6: Graph of imaginary part of Z against tension T.

Figure 3.6 illustrates the variation of the imaginary part of impedance (Im[Z]) as a function of tension T.

The x-axis represents tension values ranging from 0 to 800, while the y-axis shows the corresponding Im[Z] values, which decrease from 100 to 20. The high impedance indicates that more energy is reflected as T increases. Figure 3.7 represents the variation of the absolute part of impedance (Z) as a function of tension T. The x-axis represents tension values ranging from 0 to 800, while the y-axis shows the corresponding absolute values of Z, which decrease from 250 to 50.

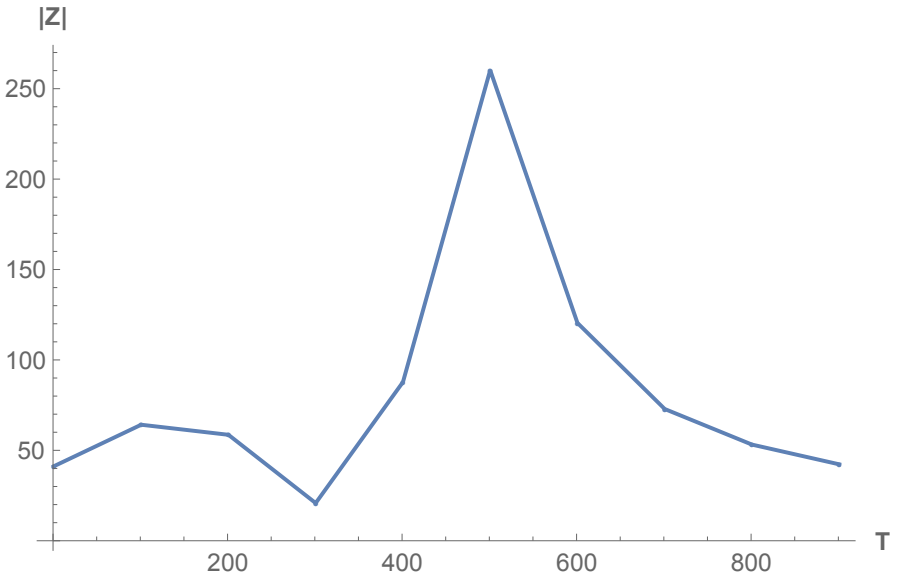

FIGURE 3.7: Graph of absolute part of Z against tension T

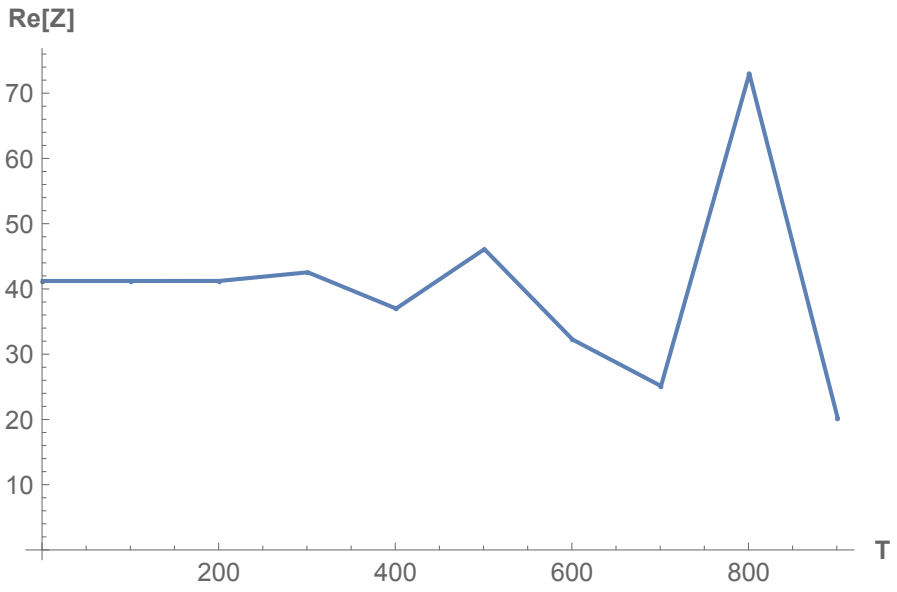

FIGURE 3.8: Graph of real part of Z against tension T.

Figure 3.8 illustrates the variation of the real part of impedance (Re[Z]) as a function of tension T. The x-axis represents tension values ranging from 0 to 800, while the y-axis shows the corresponding Re[Z] values, which decrease from 70 to 20. Figure 3.9 shows the variation of the Imaginary part of impedance (Im(Z)) as a function of tension T. The x-axis represents tension values ranging from 0 to 800, while the y-axis shows the corresponding Im(Z) values, which decrease from 40 to 10. Initially, the impedance is zero, but as the tension increases, the impedance rises, indicating that more energy is reflected.

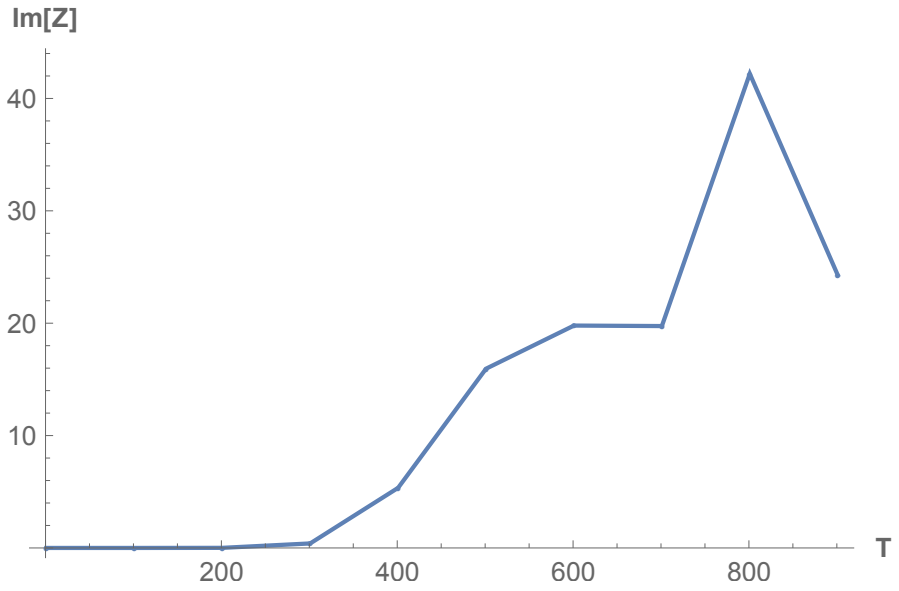

FIGURE 3.9: Graph of imaginary part of Z against tension T

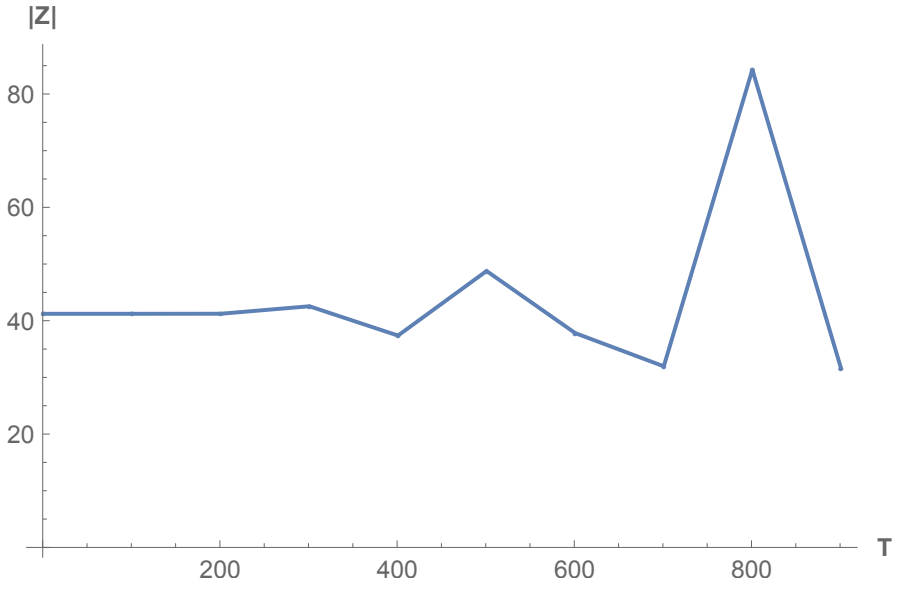

FIGURE 3.10: Graph of absolute part of Z against tension T

Figure 3.10 shows the variation of the absolute part of impedance ($|Z|$) as a function of tension T. The x-axis represents tension values ranging from 0 to 800, while the y-axis shows the corresponding absolute($|Z|$) values, which decrease from 85 to 30.

Figure 3.11 illustrates the variation of the real part of impedance (Re[Z]) as a function of tension T. The x-axis represents tension values ranging from 0 to 800, while the y-axis shows the corresponding Re[Z] values.

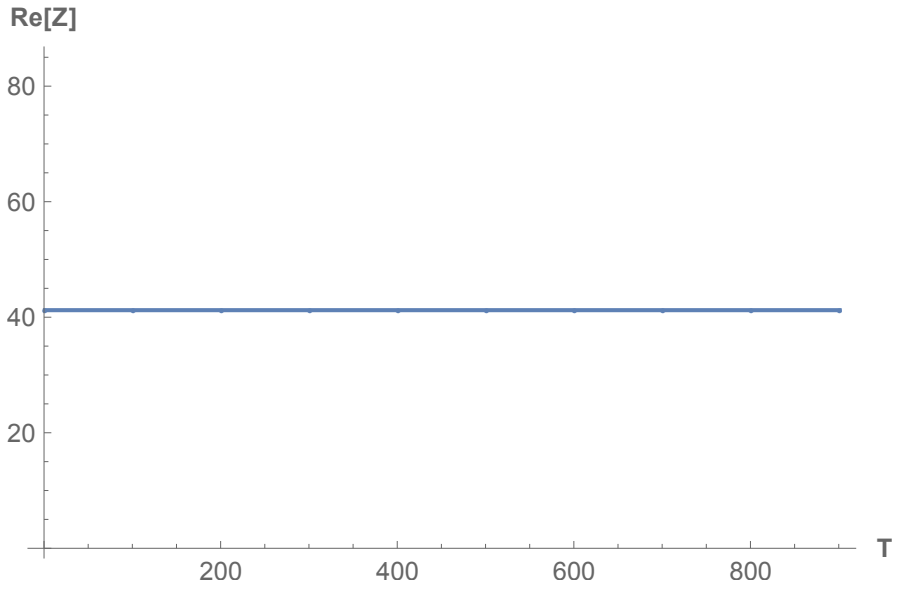

FIGURE 3.11: Graph of real part of Z against tension T.

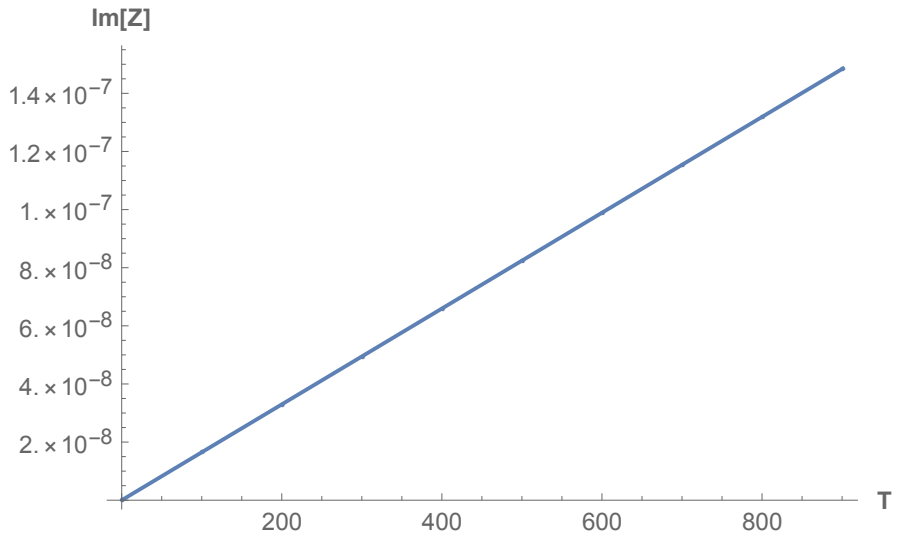

FIGURE 3.12: Graph of imaginary part of Z against tension T.

Figure 3.12 shows the variation of imaginary part of Z as a function of tension T. The x-axis represents tension values ranging from 0 to 800, while the y-axis shows the corresponding Im(Z) values, which increase from approximately $2 * 10^{-9}$ to $1.4 * 10^{-7}$. The graph indicates a significant increase in Im(Z) as tension increases.

Figure 3.13 shows the variation of the absolute part of impedance ($|Z|$) as a function of tension T. The x-axis represents tension values ranging from 0 to 800, while the y-axis shows the corresponding absolute ($|Z|$) values.

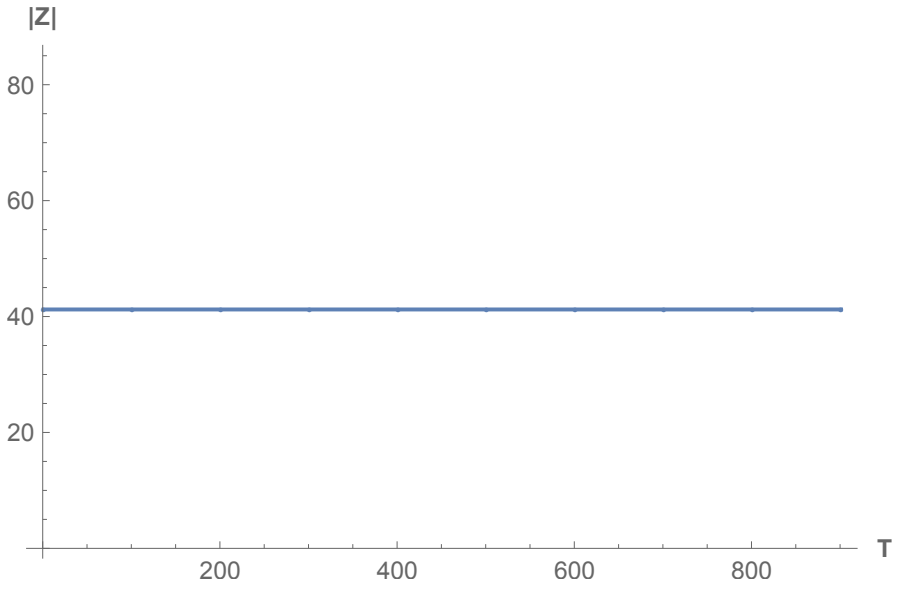

FIGURE 3.13: Graph of absolute part of Z against tension T.

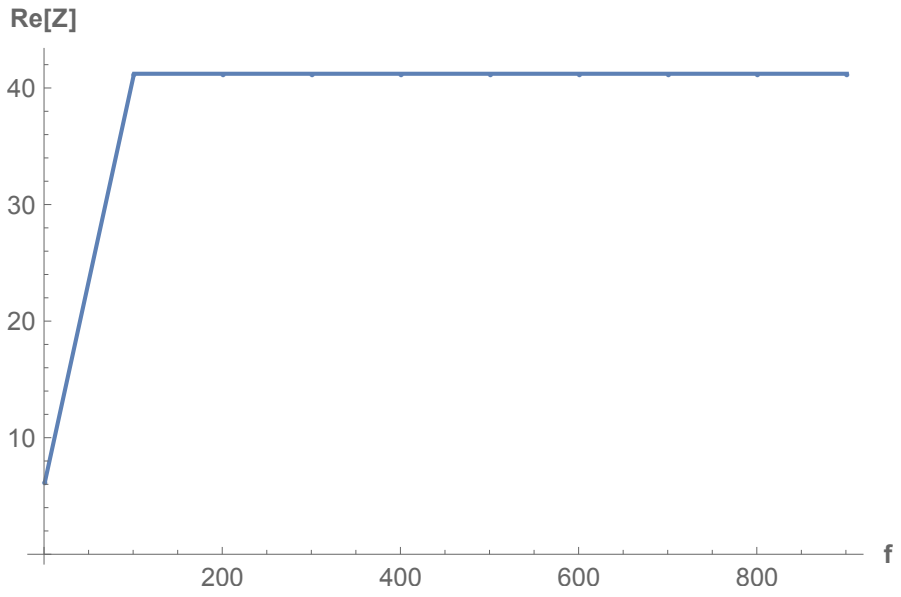

FIGURE 3.14: Graph of real part of Z against frequency f.

Figure 3.14 shows the variation of the real part of impedance with frequency f. Initially, $Re[Z]$ increases steeply with frequency and then stabilizes at a constant value. Figure 3.15 shows the imaginary component of Z as a function of frequency f. The plot indicates a sharp initial peak at lower frequencies, followed by a rapid decline to near zero for higher frequencies. This suggests that the reactance component of Z is significant at low frequencies but diminishes as frequency increases. Impedance is high at zero frequency but as frequency increases impedance is zero, which suggest resonance frequency.

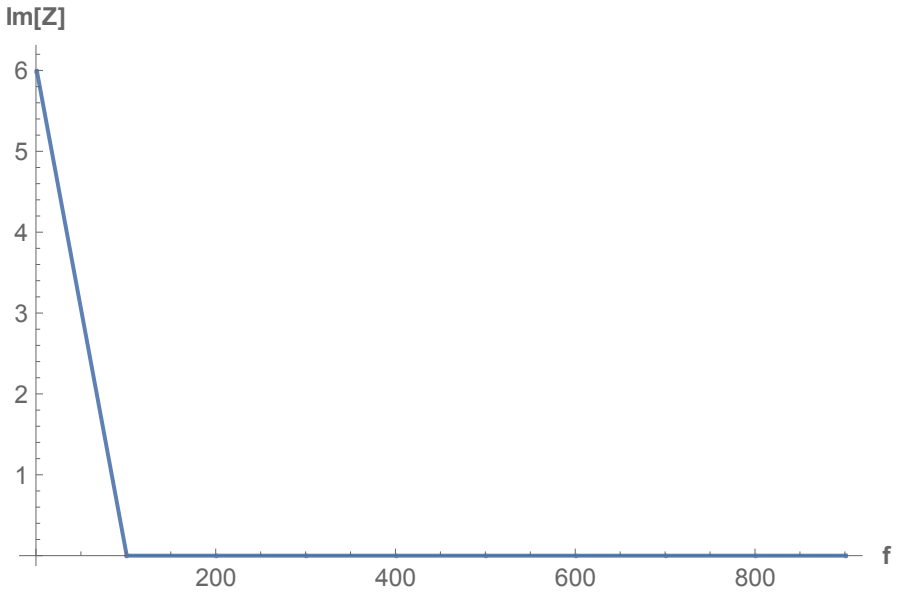

FIGURE 3.15: Graph of imaginary part of Z against frequency f.

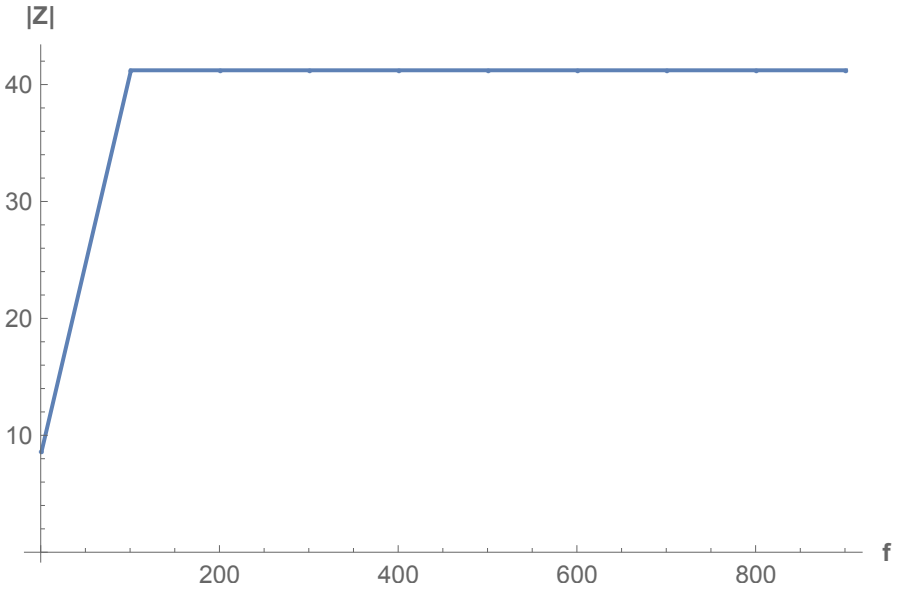

FIGURE 3.16: Graph of absolute part of Z against frequency f.

Figure 3.16 represents the absolute value of Z against frequency f. The plot shows an initial increase in absolute value of Z up to a certain frequency, after which it stabilizes and remains constant.

Figure 3.17 illustrates the variation of the real part of impedance Z as a function of frequency f. The x-axis represents the frequency f ranging from 0 to 800 units, while the y-axis represents the real part of impedance ($Re[Z]$) ranging from 0 to 70 units.

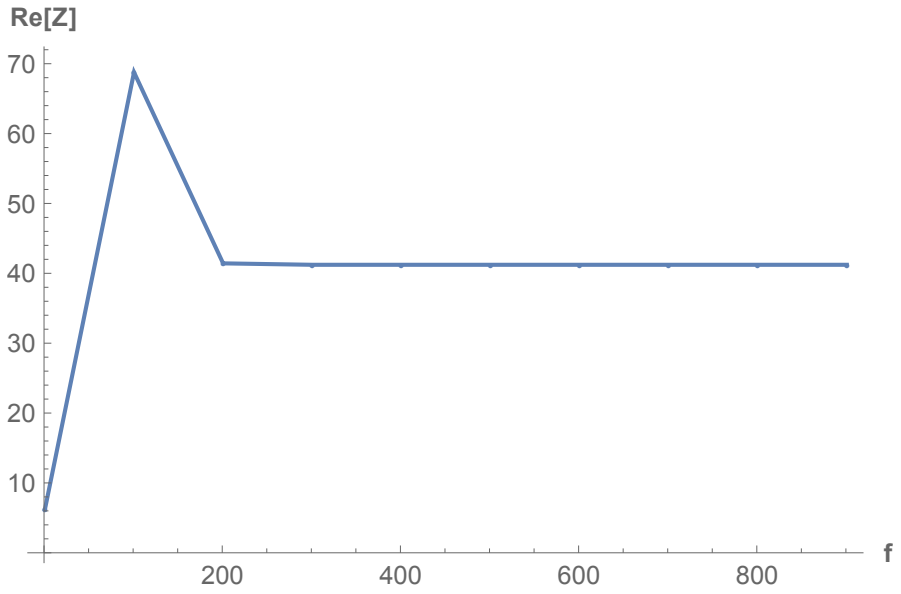

FIGURE 3.17: Graph of real part of Z against frequency f.

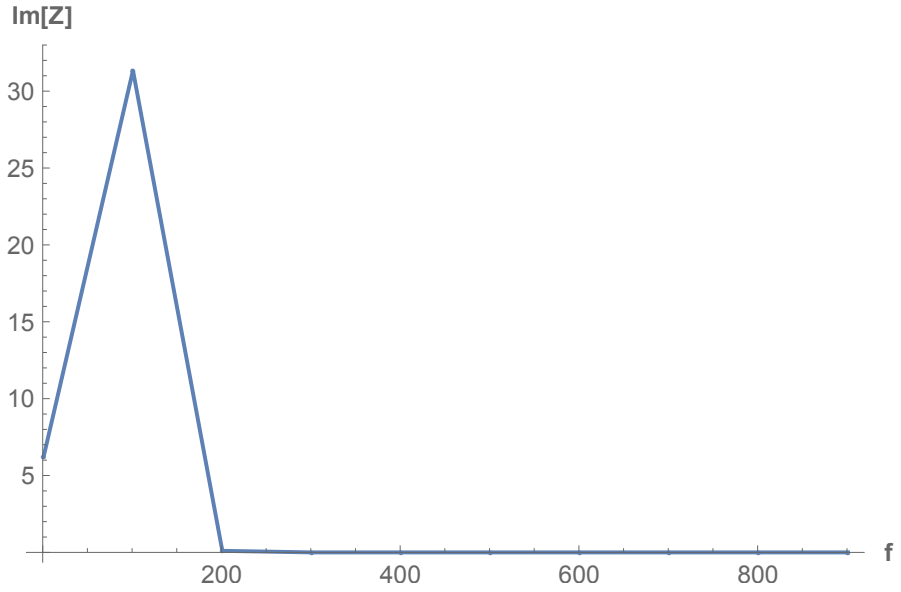

FIGURE 3.18: Graph of imaginary part of Z against frequency f.

Figure 3.18 represents the variation of the imaginary component of Z with frequency f. The plot exhibits a sharp peak at a certain frequency, indicating a resonance effect, followed by a rapid decline to zero.

Figure 3.19 illustrates the absolute value of Z as a function of frequency f. The curve shows an initial increase, reaching a peak at a specific frequency, followed by a decrease and stabilization at higher frequencies. This suggests that the impedance exhibits a resonance-like behavior before settling to a steady value.

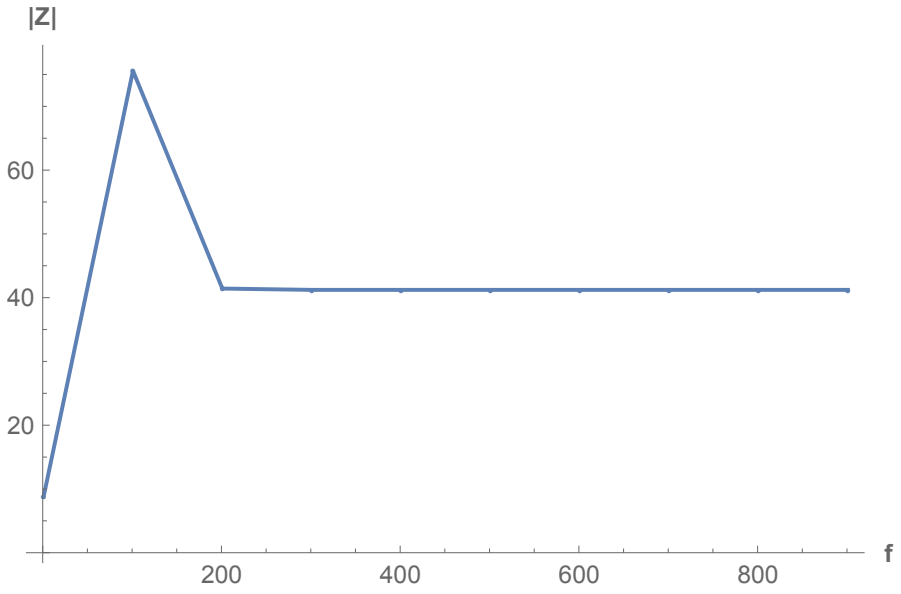

FIGURE 3.19: Graph of absolute part of Z against frequency f.

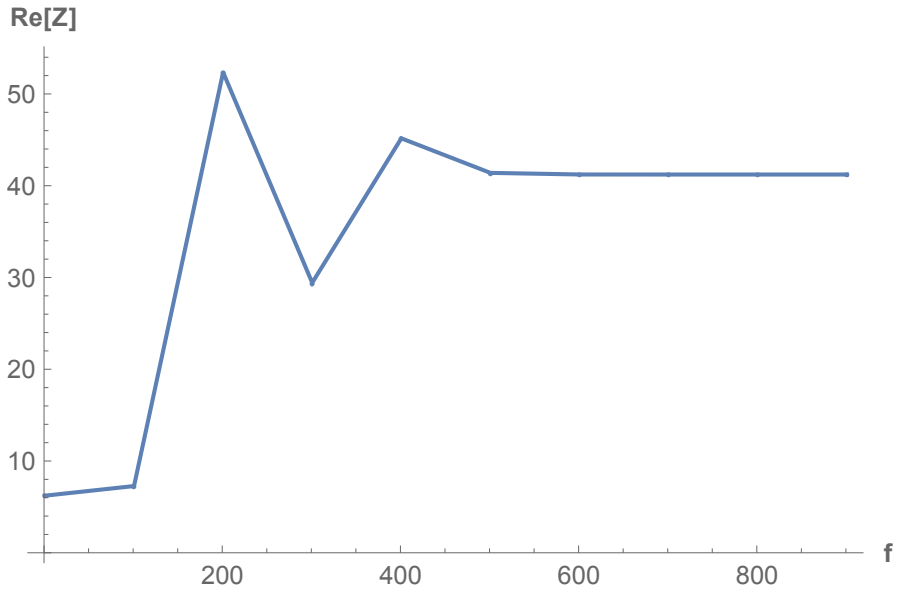

FIGURE 3.20: Graph of real part of Z against frequency f.

Figure 3.20 shows how the real part of Z varies with frequency f. Initially, $Re[Z]$ increases sharply, reaching a peak near $f \approx 200$, followed by oscillations before stabilizing at higher frequencies.

Figure 3.21 depicts the variation of the imaginary part of Z with frequency f.

Initially, $Im[Z]$ increases, reaching a peak near $f \approx 200$, and then rapidly declines, approaching zero at higher frequencies.

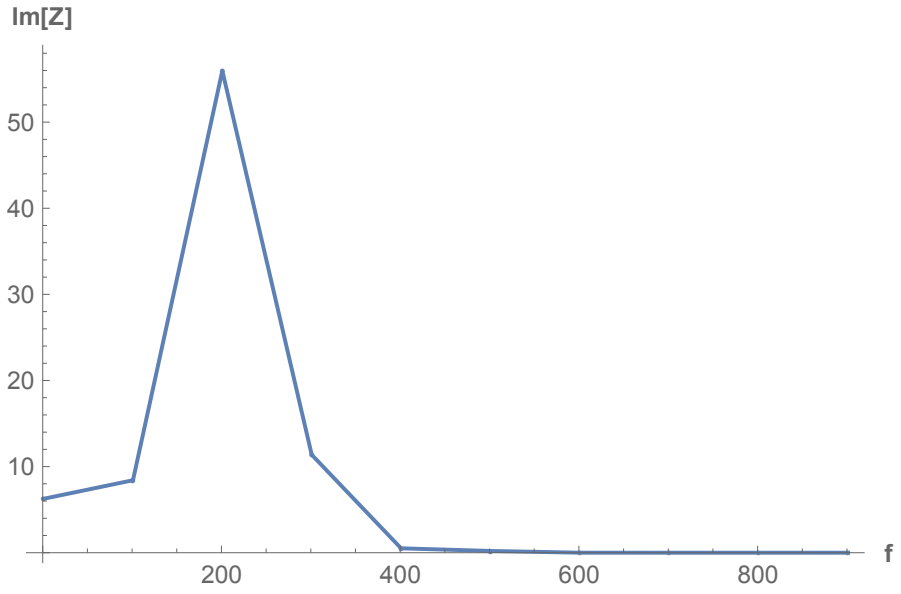

FIGURE 3.21: Graph of imaginary part of Z against frequency f.

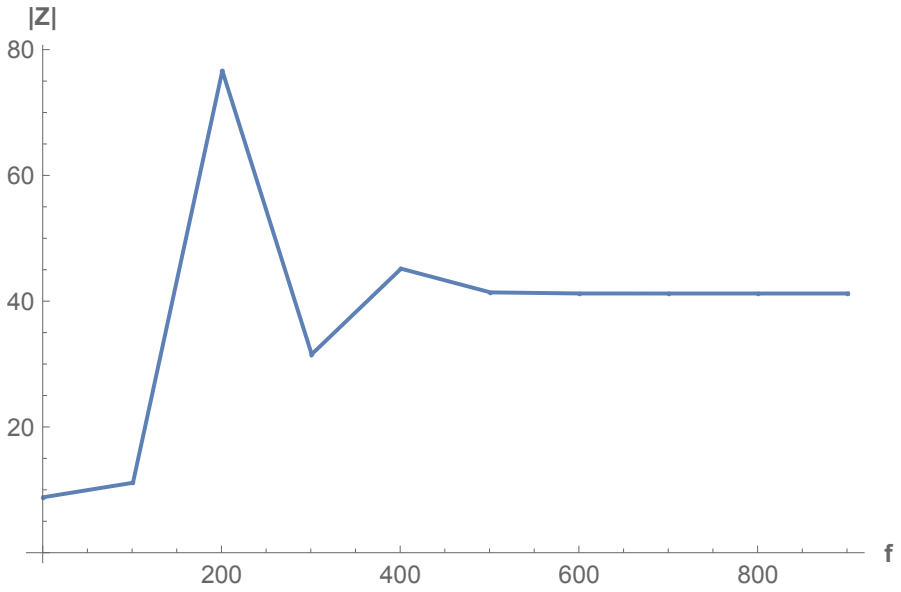

FIGURE 3.22: Graph of absolute values of Z against frequency f.

Figure 3.22 illustrates the absolute value of Z as a function of frequency f.

Initially, $|Z|$ increases sharply, reaching a peak around $f \approx 200$, followed by fluctuations before stabilizing at higher frequencies.

Figure 3.23 shows that the real part of impedance $Re(Z)$ remains constant as the parameter a varies. This suggests that the resistive component of the impedance is independent of a, indicating a stable resistance with no frequency-dependent variations or external influences affecting it.

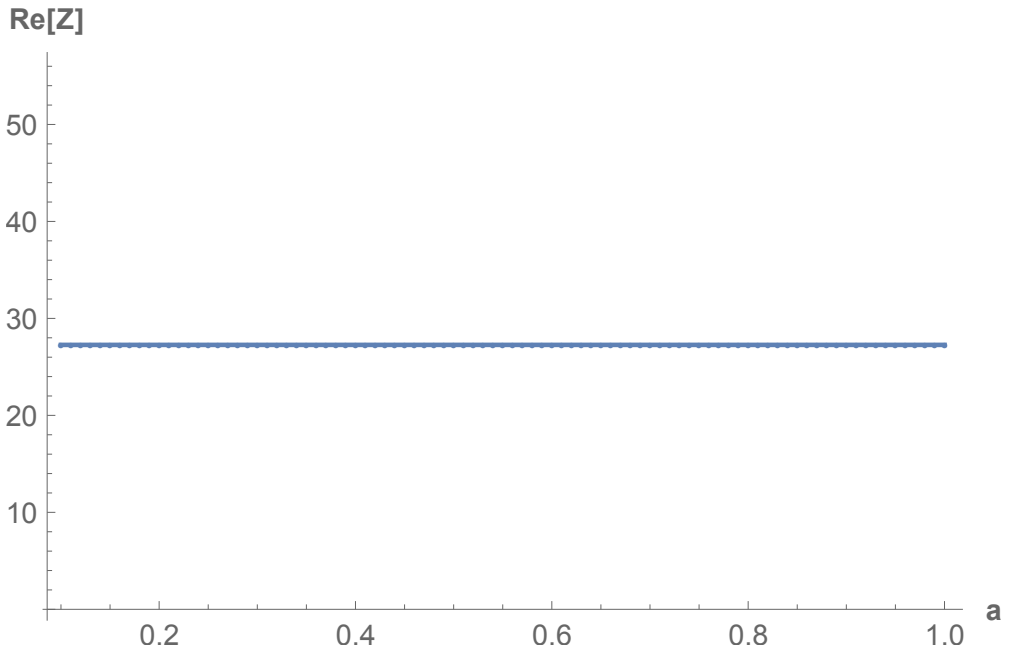

FIGURE 3.23: Graph of real values of Z against radius a.

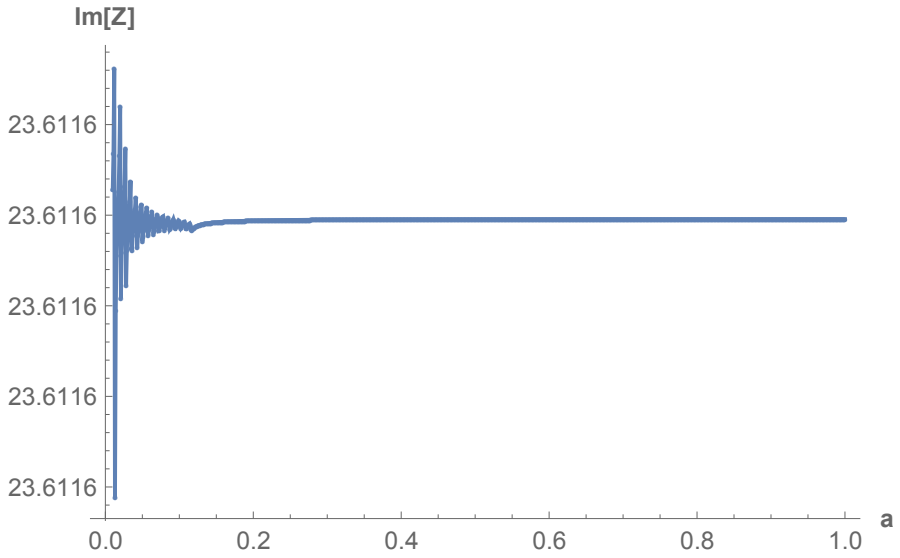

FIGURE 3.24: Graph of imaginary values of Z against radius a.

Figure 3.24 depicts the variation of the imaginary part of impedance Z with respect to a. The x-axis represents the frequency f ranging from 0 to 1, while the y-axis represents the imaginary part of impedance $(Im[Z])$. Initially, there are high-frequency oscillations that gradually dampen, leading to a steady-state value.

Figure 3.25 shows that the magnitude of impedance Z remains constant across the entire range of the parameter a.

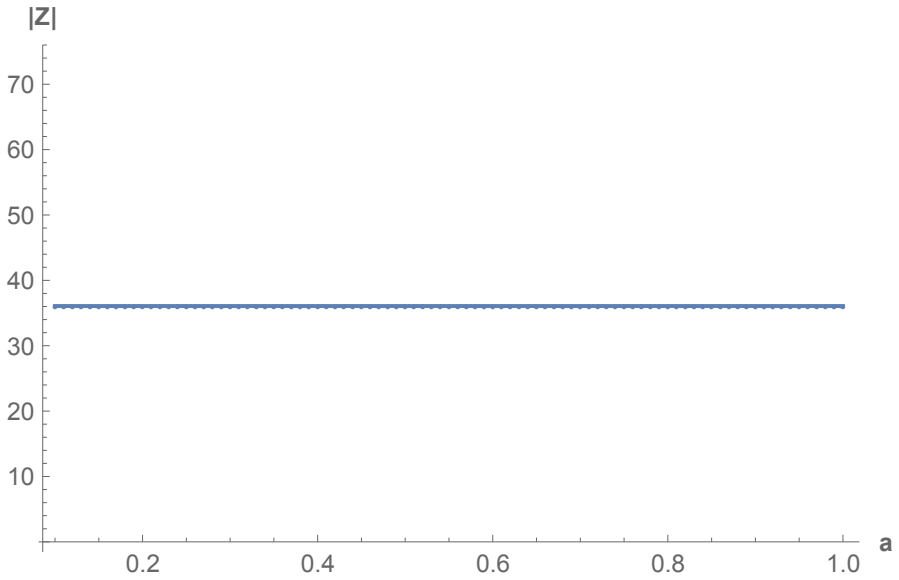

FIGURE 3.25: Graph of absolute values of Z against radius a.

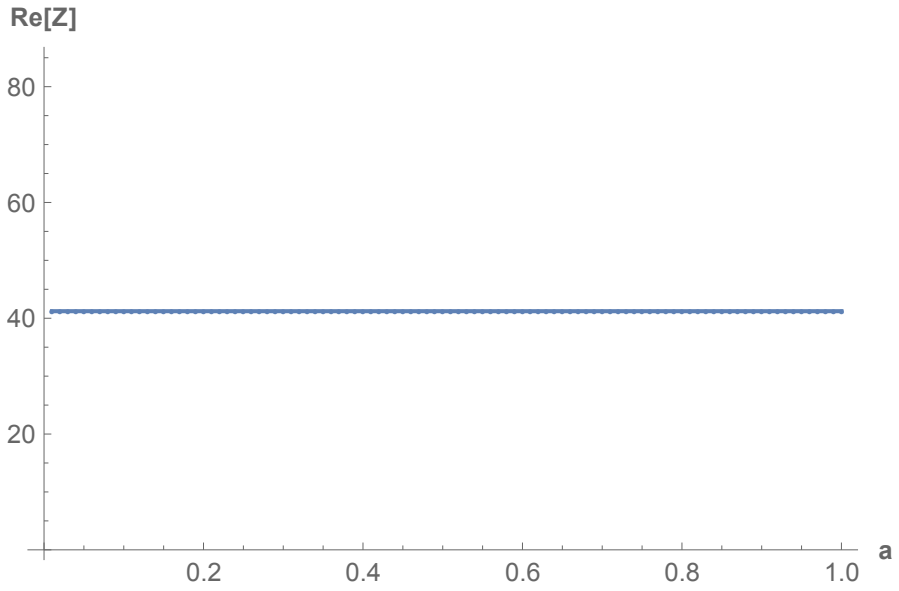

FIGURE 3.26: Graph of real values of Z against radius a.

Figure 3.26 represents the real component of Z as a function of radius a.

The plot shows a constant value of $Re[Z]$) over the entire range of a, indicating that the resistive part of the impedance does not change with radius a.

Figure 3.27 represents the imaginary component of Z as a function of a. The plot shows a steep decline at the beginning, stabilizing towards a very small constant value. This suggests that the reactive part of the impedance is initially significant but diminishes as a increases.

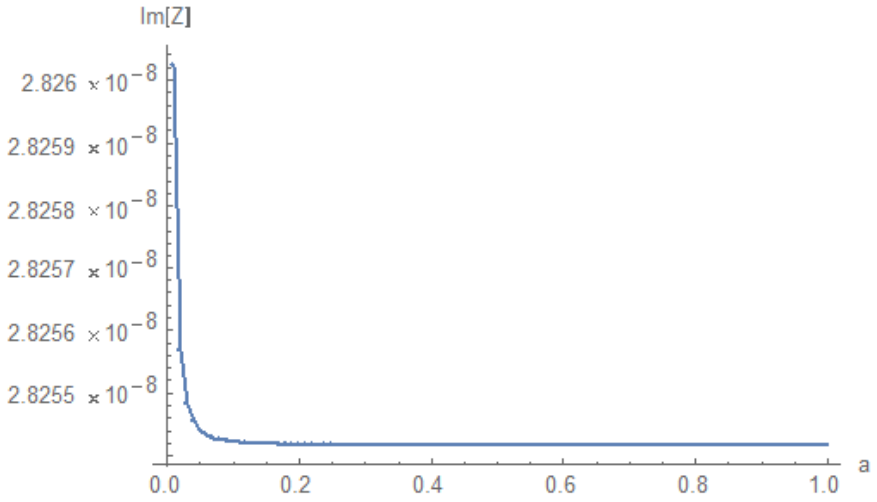

FIGURE 3.27: Graph of imaginary values of Z against radius a.

Figure 3.28 shows that the absolute value of Z remains constant as radius a varies. The flat horizontal line suggests that $|Z|$ is independent of radius a, indicating no variation in the magnitude of impedance over the given range of a.

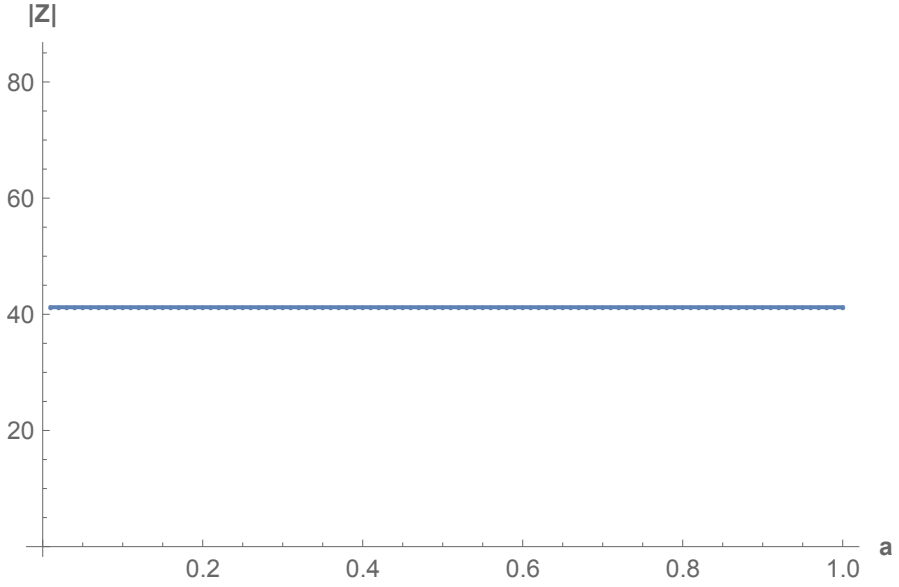

FIGURE 3.28: Graph of absolute values of Z against radius a.

3.3 Numerical Results and Discussions

Here the problem is solved analytically after making truncation of equations upto some $N = 10$ terms. The systems are solved using MATHEMATICA solver

"Solve". There are various parameters in the equations that are given numerical values. These numerical values are given in reference [38]. The particular values are taken as follows: $a = 0.1\,\mathrm{m}$, $\rho_p = 0.174$, $\rho_0 = 0.12\mathrm{kg/m}^2$, $T = 85\,\mathrm{N/m}$, $\eta = 0.005$, $f = 50$, $h = 0.2mm, d_1 = 0.05mm, d_2 = 0.08mm, c = 343.5m/s$. The number of terms are taken to 10 terms. In Figure 3.2 , the real parts of impedance are shown against radius a at frequency $f = 350$ Hz and tension $T = 880$. Figure 3.2 shows how impedance varies against radius a where the low impedance indicate more energy is absorbed. In Figure 3.23 , the real parts of impedance are shown against radius a at frequency $f = 850$ Hz and tension $T = 750$. Figure 3.23 shows that the impedance remains constant at the frequency $f = 850$. In Figure 3.26, on increasing frequency the resistive part of impedance does not change with radius a. The imaginary parts of the impedance are examined at various frequencies against tension T. The impedance results are shown in Figures. 3.6, 3.9 and 3.12 at frequencies $f = 100$, 250, and 850 Hz, respectively. At each frequency, the effect of impedance is different against tension. These results indicate that at different frequencies, as the tension increases impedance is high which suggests that more energy is reflected rather than absorbed. The Figures 3.14, 3.17 and 3.20 represent real parts of impedance against frequency f with different values of tension T. These graphs suggest that at lower frequency the system absorbed more energy but as the frequency increases it reflects sound energy rather than absorbance. The findings of this study provide valuable insights into the complex dynamics of fluid-structure interaction systems and demonstrate the effectiveness of the proposed approach in capturing these dynamics.

Chapter 4

Flexible Structure Backed By Rigid And Soft Porous Cavity

In this chapter we will study the propagation of wave with a flexible structure backed by soft porous cavity. We solve the governing boundary value problem by using the Mode Matching approach. Details of sections are as follows:

In Section 4.1, the mathematical formulation of the boundary value problem is given. In Section 4.2, We discuss the graphical results of matching conditions of problem 2. In Section 4.3, the mathematical formulation of the problem 3 is given. In Section 4.4, We discuss the graphical results of matching conditions of problem 3. In Section 4.5, We discuss the graphical results of rigid and soft porous cavity.

4.1 Mathematical Formulation

This section is extension of chapter number 3 that involves expansion chambers with absorbing lining. The physical configuration is shown in Figure 4.1,

The governing boundary value problem includes Helmholtz equation, rigid conditions and membrane conditions. For air containing regions 1 and 2, the Helmholtz equation is

$$(\nabla^2 + k^2)\phi_j(r, z) = 0, \text{for } j = 1, 2. \tag{4.1}$$

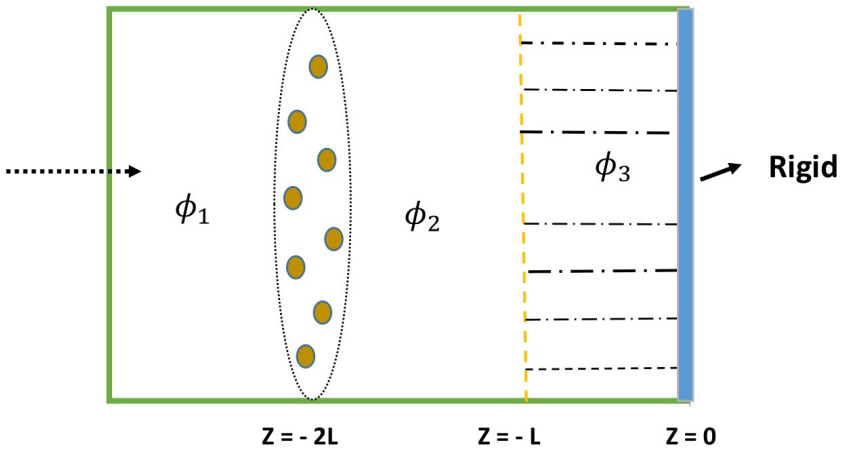

FIGURE 4.1: Physical configuration of wave guide with rigid backing

The eigenfunction in these regions is $J_0(\tau_n r)$ where τ_n are eigen-values and $\eta_n = \sqrt{k^2 - \tau_n^2}$ are mode wave number. The wave form is $(J_0(\tau_n r)e^{\overset{+}{-}i\eta_n z}$.

For Porosity containing region, the Helmholtz equation is

$$(\nabla^2 + \Gamma^2)\phi_3(r, z) = 0. \tag{4.2}$$

The eigenfunction in this region is $J_0(\tau_n r)$ where τ_n are eigenvalues and $S_n = \sqrt{\Gamma^2 - \tau_n^2}$ are mode wave number.

The wave form is $J_0(\tau_n r)e^{\overset{+}{-}i\Gamma_n Z}$.

4.1.1 The Eigenfunction Expansion Forms For Flexible Structure Backed By Rigid Porous Cavity

In symmetric settings, the eigenfunction expansion represents a function in terms of eigenfunctions of an operator that respects the symmetry of the domain.

This form exploits the problem's symmetry to reduce complexity, leading to an efficient way to solve boundary value problems. Symmetry simplifies the problem by reducing the number of independent variables or transforming the problem into a simpler form.

The eigenfunction expansion forms for symmetric setting are

$$\phi_1^s(r,z) = e^{ik(z+2L)} + \sum_{n=0}^{\infty} A_n^s J_0(\tau_n r) e^{-i\eta_n(z+2L)}. \tag{4.3}$$

$$\phi_2^s(r,z) = \sum_{n=0}^{\infty} \left[B_n^s e^{i\eta_n(z+L)} + C_n^s e^{-i\eta_n(z+L)}\right] J_0(\tau_n r). \tag{4.4}$$

$$\phi_3^s(r,z) = 2\sum_{n=0}^{\infty} \left[D_n^s \cos(s_n z)\right] J_0(\tau_n r), \tag{4.5}$$

where $\eta_n = \sqrt{k^2 - \tau_n^2}$ and $s_n = \sqrt{\Gamma^2 - \tau_n^2}$ for n=0,1,2,... The coefficients $\{A_n^s, C_n^s\}$ for n = 0, 1 ,2 ,..., are the amplitudes of n^{th} reflected duct modes and the coefficients $\{B_n^s, D_n^s\}$ for n = 0, 1, 2,..., are the amplitudes of n^{th} transmitted duct modes. As these modal coefficients are unknowns and we determine these unknowns by using mode matching technique.

4.1.2 For Membrane Response at $Z = -2L$

The equation of motion for membrane vibration is

$$(\nabla^2 + k_p^2) W_1(r) = \alpha_p(\phi_2^s - \phi_1^s), \tag{4.6}$$

with the boundary condition that the membrane is fixed at the edge

$$W_1(a) = 0. \tag{4.7}$$

Assume the solution of the form

$$W_1(r) = \sum_{n=0}^{\infty} U_n J_0(\lambda_n r), \tag{4.8}$$

such that (4.8) satisfies the equation associated with equation (4.6) and boundary condition (4.7). Here λ_n are roots of $J_0(\lambda_n a) = 0$ and $J_0(\lambda_n r)$ satisfy the orthogonality relation,

$$\int_0^a J_0(\lambda_n r) J_0(\lambda_m r) r dr = \delta_{mn} I_m, \tag{4.9}$$

where δ_{mn} is a kronecker delta and

$$I_m = \begin{cases} 1, & \text{if } m = 0, \\ 0, & \text{otherwise.} \end{cases}$$

To find U_n, we use (4.3), (4.4) and (4.8) into (4.6), we get

$$(\nabla^2 + k_p^2)\sum_{n=0}^{\infty} U_n J_0(\lambda_n r) = \alpha_p \Bigg[\sum_{n=0}^{\infty} \{B_n^s e^{i\eta_n(z+L)} + C_n^s e^{-i\eta_n(z+L)}\} J_0(\tau_n r) - e^{ik(z+2L)} - \sum_{n=0}^{\infty} A_n^s J_0(\tau_n r) e^{-i\eta_n(z+2L)} \Bigg],$$

or

$$\sum_{n=0}^{\infty} U_n (k_p^2 - \lambda_n^2) J_0(\lambda_n r) = \alpha_p \Big[\sum_{n=0}^{\infty} \{B_n^s e^{-i\eta_n L} + C_n^s e^{i\eta_n L}\} J_0(\tau_n r) - 1 - \sum_{n=0}^{\infty} A_n^s J_0(\tau_n r) \Big]. \tag{4.10}$$

Upon substituting $z = -2L$ into (4.10), we obtain

$$(\nabla^2 + k_p^2)\sum_{n=0}^{\infty} U_n J_0(\lambda_n r) = \alpha_p \Big[\sum_{n=0}^{\infty} \{B_n^s e^{-i\eta_n L} + C_n^s e^{i\eta_n L}\} J_0(\tau_n r) - 1 - \sum_{n=0}^{\infty} A_n^s J_0(\tau_n r) \Big]. \tag{4.11}$$

Multiplying both sides by $rJ_0(\lambda_m r)$ and integrating over the range from 0 to a leads to

$$\sum_{n=0}^{\infty} U_n (k_p^2 - \lambda_n^2) \int_0^a J_0(\lambda_n r) J_0(\lambda_m r) r dr = \alpha_p \Big[\sum_{n=0}^{\infty} \{B_n^s e^{-i\eta_n L} + C_n^s e^{i\eta_n L}\} \int_0^a J_0(\tau_n r) J_0(\lambda_m r) r dr - \int_0^a J_0(\lambda_m r) r dr - \sum_{n=0}^{\infty} A_n^s \int_0^a J_0(\tau_n r) J_0(\lambda_m r) r dr \Big]. \tag{4.12}$$

By using (4.9) and orthogonality relation into (4.12), we obtain

$$U_m (k_p^2 - \lambda_m^2) I_m = \alpha_p \Big[\sum_{n=0}^{\infty} \{B_n^s e^{-i\eta_n L} + C_n^s e^{i\eta_n L}\} R_{mn} - \delta_{m0} - \sum_{n=0}^{\infty} A_n^s R_{mn} \Big],$$

or

$$U_m = \frac{\alpha_p}{(k_p^2 - \lambda_m^2)I_m}\Big[\sum_{n=0}^{\infty}\{B_n^s e^{-i\eta_n L} + C_n^s e^{i\eta_n L} - A_n^s\}R_{mn} - \delta_{m0}\Big]. \tag{4.13}$$

On matching the velocities across the regions at interface $z = -L$, the continuity condition of velocity at $z = -L$ can be expressed as:

$$\frac{\partial \phi_2^s}{\partial z} = \frac{\partial \phi_3^s}{\partial z}. \tag{4.14}$$

Upon using (4.4) and (4.5) into (4.14), we have

$$\sum_{n=0}^{\infty}\Big[B_n^s(i\eta_n) + C_n^s(-i\eta_n)\Big]J_0(\tau_n r) = -2s_m\sum_{n=0}^{\infty}D_n^s\sin(s_nL)J_0(\tau_n r).$$

Multiplying both sides by $rJ_0(\tau_m r)$ and integrating from 0 to a, we get

$$\sum_{n=0}^{\infty}\Big[B_n^s(i\eta_n) - C_n^s(i\eta_n)\Big]\int_0^{\infty}J_0(\tau_n r)J_0(\tau_m r)rdr = -2s_m\sum_{n=0}^{\infty}D_n^s\sin(s_nL)\int_0^a J_0(\tau_n r)J_0(\tau_m r)rdr.$$

By using orthogonality relation, we obtain,

$$B_m^s - C_m^s = -\frac{2s_m}{i\eta_m R_m}D_m^s\sin(s_mL). \tag{4.15}$$

The continuity condition at $z = -L$ is

$$\phi_2^s(r,-L) = \beta\phi_3^s(r,-L). \tag{4.16}$$

On using (4.4) and (4.5) into (4.16), we have

$$\sum_{n=0}^{\infty}\Big[B_n^s + C_n^s\Big]J_0(\tau_n r) = 2\beta\sum_{n=0}^{\infty}D_n^s\cos(s_nL)J_0(\tau_n r).$$

Multiplying both sides by $rJ_0(\tau_m r)$ and integrate from 0 to a, we get

$$\sum_{n=0}^{\infty}\Big[B_n^s + C_n^s\Big]\int_0^{\infty} J_0(\tau_n r)J_0(\tau_m r)rdr = 2\beta\sum_{n=0}^{\infty} D_n^s\cos(s_n L)\int_0^a J_0(\tau_n r)J_0(\tau_m r)rdr. \tag{4.17}$$

By using orthogonality relation into (4.17), we can write B_m^s and C_m^s in the form of D_m^s as

$$B_m^s + C_m^s = 2\beta D_m^s\cos(s_m L). \tag{4.18}$$

By adding (4.15) and (4.18), we get

$$2B_m^s = 2\beta D_m^s\cos(s_m L) - \frac{2s_m}{i\eta_m R_m}D_m^s\sin(s_m L),$$

or

$$B_m^s = \Big[\beta\cos(s_m L) + \frac{is_m}{\eta_m R_m}\sin(s_m L)\Big]D_m^s. \tag{4.19}$$

By subtracting (4.15) and (4.18), we get

$$2C_m^s = 2\beta D_m^s\cos(s_m L) + \frac{2s_m}{i\eta_m R_m}D_m\sin(s_m L),$$

or

$$C_m^s = \Big[\beta\cos(s_m L) - \frac{is_m}{\eta_m R_m}\sin(s_m L)\Big]D_m^s. \tag{4.20}$$

The continuity condition of velocity at $z = -2L$ can be expressed as

$$\frac{\partial\phi_1^s}{\partial z} = W_1(r).$$

Upon using (4.3) at $z = -2L$, we have

$$e^{ik(z+2L)}(ik) + \sum_{n=0}^{\infty} A_n^s J_0(\tau_n r)e^{-i\eta_n(z+2L)}(-i\eta_n) = \sum_{n=0}^{\infty} U_n J_0(\lambda_n r).$$

Multiplying both sides by $rJ_0(\tau_m r)$ and integrating from 0 to a, we obtain

$$ik\int_0^a J_0(\tau_m r)rdr+\sum_{n=0}^{\infty}A_n^s(-i\eta_n)\int_0^{\infty}J_0(\tau_n r)J_0(\tau_m r)rdr=\sum_{n=0}^{\infty}U_n\int_0^a J_0(\lambda_n r)J_0(\lambda_m r)rdr. \tag{4.21}$$

By using orthogonality relation, we get

$$A_m^s=\frac{k\delta_{mo}}{\eta_m}+\frac{i}{\eta_m R_m}\sum_{n=0}^{\infty}U_n R_{mn}. \tag{4.22}$$

The continuity condition of velocity is $\partial\phi_2^s/\partial z=W_1(r)$ at $z=-2L$.
On using (4.4) and (4.10), we have

$$\sum_{n=0}^{\infty}\left[B_n^s e^{-i\eta_n L}(i\eta_n)+C_n^s e^{i\eta_n L}(-i\eta_n)\right]J_0(\tau_n r)=\sum_{n=0}^{\infty}U_n J_0(\lambda_n r).$$

Multiplying both sides by $rJ_0(\tau_m r)$ and integrating from 0 to a, we get

$$\sum_{n=0}^{\infty}i\eta_n\left[B_n^s e^{-i\eta_n L}-C_n^s e^{i\eta_n L}\right]\int_0^a J_0(\tau_n r)J_0(\tau_m r)rdr=\sum_{n=0}^{\infty}U_m\int_0^a J_0(\lambda_n r)J_0(\tau_m r)rdr.$$

Since Bessel's functions of the first kind $J_0(\tau_n r)$, form an orthogonal set over the interval $[0,a]$ with respect to r. So the orthogonality condition for Bessel functions $J_0(\tau_n r)$ is given by

$$\int_0^a J_0(\tau_n r)J_0(\tau_m r)\,r\,dr=\begin{cases}0 & \text{if } n\neq m,\\ \frac{a^2}{2}[J_1(\tau_n a)]^2 & \text{if } n=m,\end{cases}$$

where τ_n are the roots of $J_0(\tau_n a)=0$, and J_1 is the Bessel function of the first kind of order one.

By using orthogonality relation, we get

$$B_m^s e^{-i\eta_m L}-C_m^s e^{i\eta_m L}=\frac{-i}{\eta_m R_m}\sum_{n=0}^{\infty}U_n R_{mn}. \tag{4.23}$$

4.2 Graphical Results of Problem 2

In this section, we present and analyze the graphical results for the real and imaginary parts of velocities in a porous medium adjacent to a rigid wall. The velocity components have been computed by solving the governing equations, and the solution is truncated to 15 terms to validate the matching conditions across different regions. The results confirm that the velocity field is continuous across three region. The accuracy of the truncation method is validated as no significant deviation is observed. The continuity of the imaginary velocity components across the medium suggests a correct application of boundary conditions. The real and imaginary velocity components are in good agreement with theoretical predictions. Figures 4.2 - 4.5 confirm the validity of the solution in the presence of a rigid wall at the back of the porous medium.

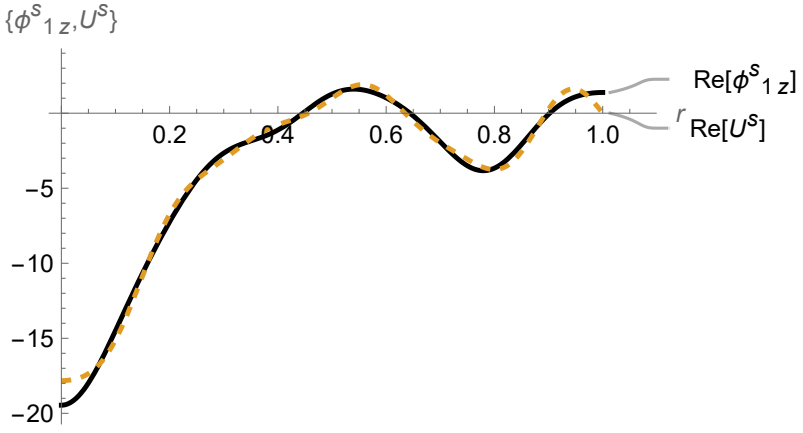

FIGURE 4.2: For rigid wall: The real parts of velocities ϕ^s_{1z} and U^s against radius r at $z = -2L$ with 15 terms.

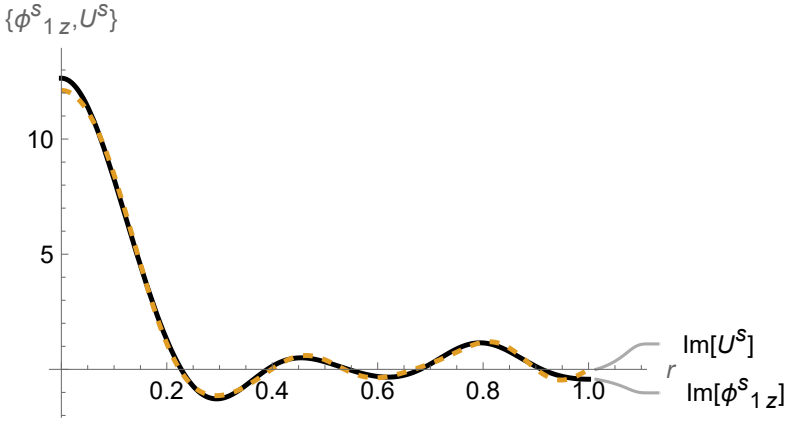

FIGURE 4.3: For rigid wall: The imaginary parts of velocities ϕ^s_{1z} and U^s against radius r at $z = -2L$ with 15 terms.

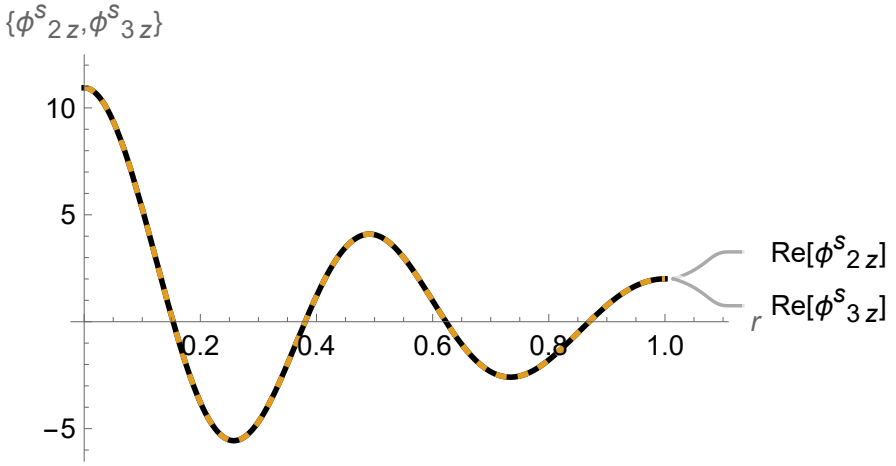

FIGURE 4.4: For rigid wall: The real parts of velocities ϕ^s_{2z} and ϕ^s_{3z} against radius r at $z = -L$ with 15 terms.

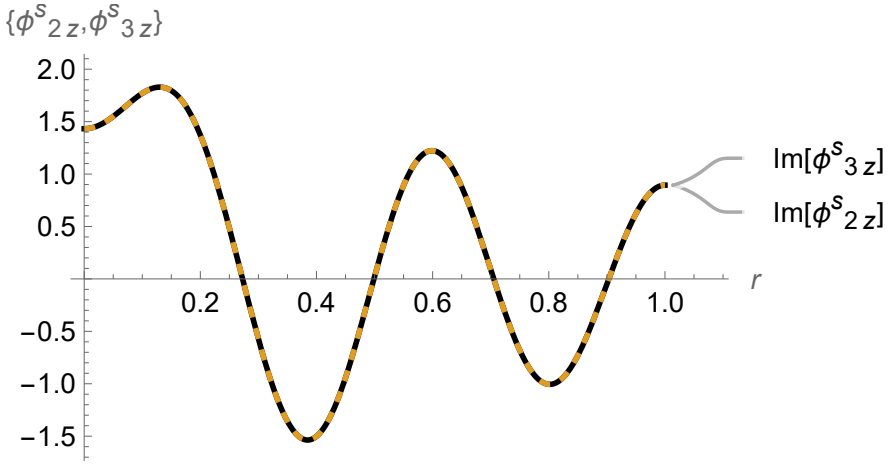

FIGURE 4.5: For rigid wall: The imaginary parts of velocities ϕ^s_{2z} and ϕ^s_{3z} against radius r at $z = -L$ with 15 terms.

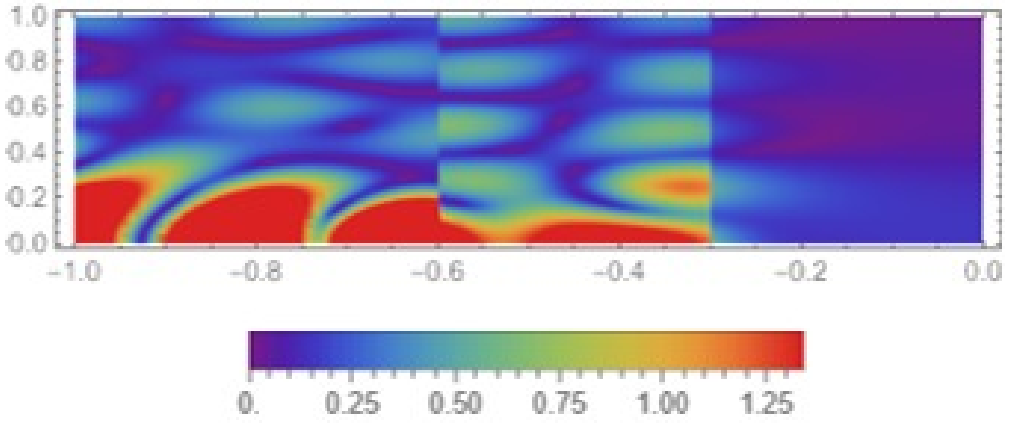

FIGURE 4.6: For symmetric case: The density plots in whole domain $-1 < z < 0$ and $0 < r < a$ while $a = 1, L = -0.3$.

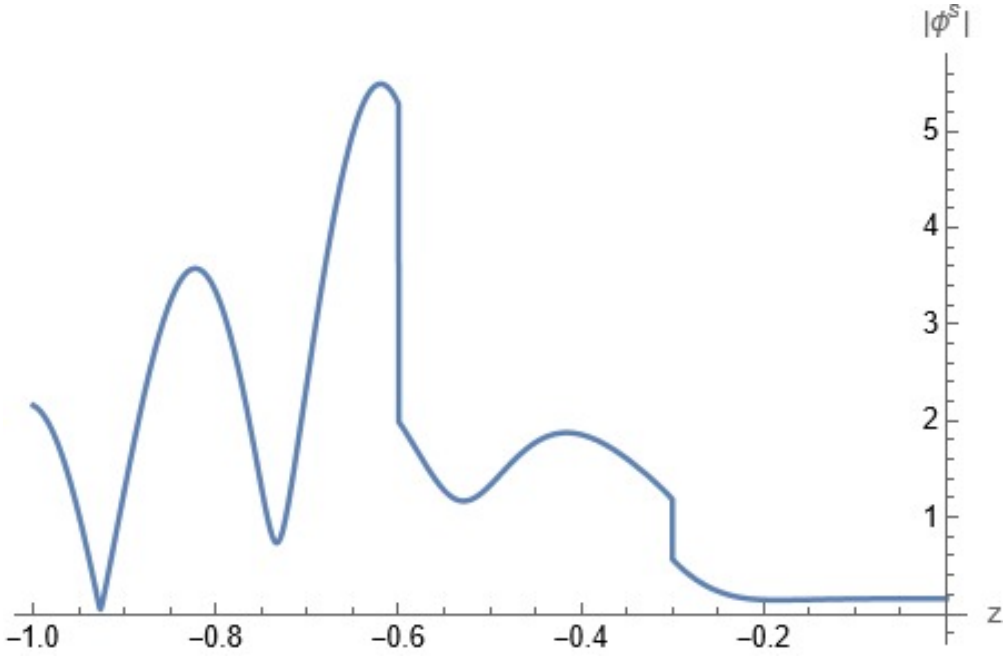

FIGURE 4.7: For symmetric case: The graph of absolute value of ϕ^s against z while $-1 < z < 0$, where $L = -0.3, f = 1000, r = 0$.

Figure 4.6 is the density plot for symmetric case that is for rigid wall with $L = -0.3$. The horizontal line represent z, ranging from -1 to -0.6 and the vertical line represent r, ranging from 0 to 1. The colored shown in Figure 4.6 represent the third dimension.

4.3 The Eigenfunction Expansion Forms For Flexible Structure Backed By Soft Porous Cavity

In an anti-symmetric setting, the eigenfunction expansion differs from symmetric settings due to the behavior of the eigenfunctions under certain transformations, such as reflection or inversion. In anti-symmetric settings, the eigenfunction expansion represents a function as a sum of eigenfunctions that satisfy anti-symmetric boundary conditions. These eigenfunctions are typically odd functions and the expansion uses orthogonality relations to determine the coefficients. Anti-symmetry typically refers to functions or solutions that change sign under a specific symmetry transformation as shown in Figure 4.8.

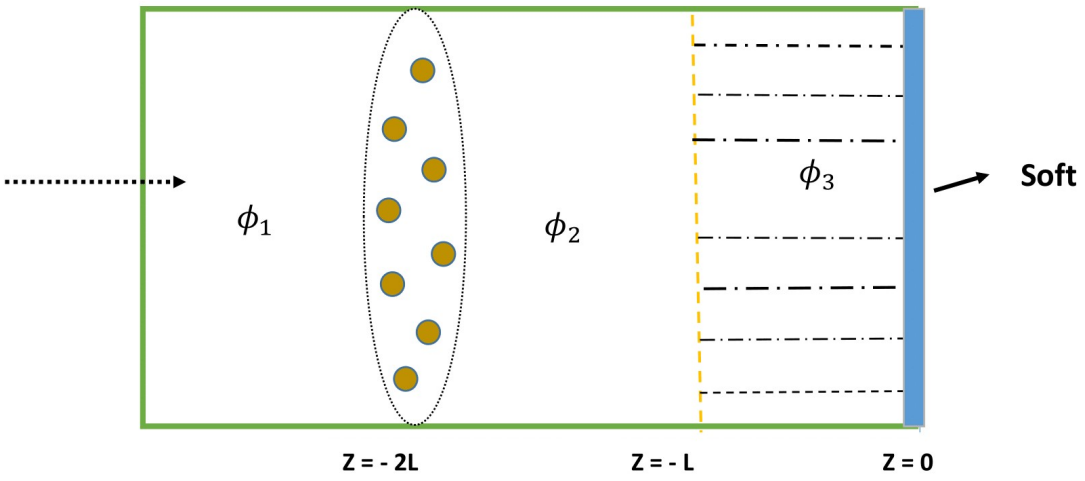

FIGURE 4.8: Physical configuration of waveguide with soft backing

$$\phi_1^a(r,z) = e^{ik(z+2L)} + \sum_{n=0}^{\infty} A_n^a J_0(\tau_n r) e^{-i\eta_n(z+2L)}. \tag{4.24}$$

$$\phi_2^a(r,z) = \sum_{n=0}^{\infty} \left[B_n^a e^{i\eta_n(z+L)} + C_n^a e^{-i\eta_n(z+L)}\right] J_0(\tau_n r). \tag{4.25}$$

$$\phi_3^a(r,z) = 2i \sum_{n=0}^{\infty} \left[D_n^a \sin(s_n z)\right] J_0(\tau_n r), \tag{4.26}$$

where $\eta_n = \sqrt{k^2 - \tau_n^2}$ and $s_n = \sqrt{\Gamma^2 - \tau_n^2}$ for $n = 0, 1, 2, \ldots$.

The coefficients $\{A_n^a, C_n^a\}$ for $n = 0, 1, 2, ...,$ are the amplitudes of n^{th} reflected duct modes and the coefficients $\{B_n^a, D_n^a\}$ for $n = 0, 1, 2, ...,$ are the amplitudes of n^{th} transmitted duct modes. As these modal coefficients are unknowns and we determine these unknowns by using mode matching technique.

4.3.1 For Membrane Response at $z = -2L$

The equation of motion for membrane vibration is given by

$$(\nabla^2 + k_p^2) W_1(r) = \alpha_p(\phi_2^a - \phi_1^a), \tag{4.27}$$

with the boundary condition that the membrane is fixed at the edge

$$W_1(a) = 0. \tag{4.28}$$

Assume the solution of the form

$$W_1(r) = \sum_{n=0}^{\infty} U_n J_0(\lambda_n r), \tag{4.29}$$

where (4.29) satisfies the equation associated with (4.27) and boundary condition (4.28). Here λ_n are roots of $J_0(\lambda_n a) = 0$ and $J_0(\lambda_n r)$ satisfy the orthogonality relation

$$\int_0^a J_0(\lambda_n r) J_0(\lambda_m r) r dr = \delta_{mn} I_m, \tag{4.30}$$

where δ_{mn} is the kronecker delta.

To find U_n , use (4.24), (4.25) and (4.29) into (4.27), we have

$$(\nabla^2 + k_p^2) \sum_{n=0}^{\infty} U_n J_0(\lambda_n r) = \alpha_p \Bigg[\sum_{n=0}^{\infty} \left\{ B_n^a e^{i\eta_n (z+L)} + C_n^a e^{-i\eta_n (z+L)} \right\} J_0(\tau_n r) - e^{ik(z+2L)} - \sum_{n=0}^{\infty} A_n^a J_0(\tau_n r) e^{-i\eta_n (z+2L)} \Bigg].$$

Upon substituting $z = -2L$, we get

$$(\nabla^2 + k_p^2) \sum_{n=0}^{\infty} U_n J_0(\lambda_n r) = \alpha_p \Big[\sum_{n=0}^{\infty} \{ B_n^a e^{-i\eta_n L} + C_n^a e^{i\eta_n L} \} J_0(\tau_n r) - 1 - \sum_{n=0}^{\infty} A_n^a J_0(\tau_n r) \Big], \tag{4.31}$$

or

$$\sum_{n=0}^{\infty} U_n (k_p^2 - \lambda_n^2) J_0(\lambda_n r) = \alpha_p \Big[\sum_{n=0}^{\infty} \{ B_n^a e^{-i\eta_n L} + C_n^a e^{i\eta_n L} \} J_0(\tau_n r) - 1 - \sum_{n=0}^{\infty} A_n^a J_0(\tau_n r) \Big].$$

Multiplying both sides by $r J_0(\lambda_m r)$ and integrating from 0 to a , we obtain

$$\sum_{n=0}^{\infty} U_n(k_p^2-\lambda_n^2)\int_0^a J_0(\lambda_n r)J_0(\lambda_m r)rdr = \alpha_p\Big[\sum_{n=0}^{\infty}\{B_n^a e^{-i\eta_n L}+C_n^a e^{i\eta_n L}\}$$
$$\int_0^a J_0(\tau_n r)J_0(\lambda_m r)rdr - \int_0^a J_0(\lambda_m r)rdr - \sum_{n=0}^{\infty} A_n^a\int_0^a J_0(\tau_n r)J_0(\lambda_m r)rdr\Big].$$

By using (4.25) and orthogonality relation, we get

$$U_m(k_p^2-\lambda_m^2)I_m = \alpha_p\Big[\sum_{n=0}^{\infty}\{B_n^a e^{-i\eta_n L}+C_n^a e^{i\eta_n L}\}R_{mn}-\delta_{m0}-\sum_{n=0}^{\infty}A_n^a R_{mn}\Big],$$

or

$$U_m = \frac{\alpha_p}{(k_p^2-\lambda_m^2)I_m}\Big[\sum_{n=0}^{\infty}\{B_n^a e^{-i\eta_n L}+C_n^a e^{i\eta_n L}-A_n^a\}R_{mn}-\delta_{m0}\Big]. \tag{4.32}$$

On matching the velocities across the regions at interface $z=-L$, the continuity condition at $z=-L$ is

$$\frac{\partial\phi_2^a}{\partial z} = \frac{\partial\phi_3^a}{\partial z}.$$

Upon using (4.25) and (4.26), we have

$$\sum_{n=0}^{\infty}\Big[B_n^a(i\eta_n)+C_n^a(-i\eta_n)\Big]J_0(\tau_n r) = 2is_n\sum_{n=0}^{\infty}D_n^a\cos(s_nL)J_0(\tau_n r).$$

Multiplying both sides by $rJ_0(\tau_m r)$ and integrating from 0 to a , we obtain

$$\sum_{n=0}^{\infty}\Big[B_n^a(i\eta_n)-C_n^a(i\eta_n)\Big]\int_0^{\infty}J_0(\tau_n r)J_0(\tau_m r)rdr =$$
$$2s_n\sum_{n=0}^{\infty}D_n^a\cos(s_nL)\int_0^a J_0(\tau_n r)J_0(\tau_m r)rdr.$$

By using orthogonality relation, we get

$$B_m^a - C_m^a = \frac{2s_m}{\eta_m R_m}D_m^a\cos(s_mL). \tag{4.33}$$

The continuity condition at $z=-L$ is;

$$\phi_2^a(r,-L) = \beta\phi_3^a(r,-L).$$

Upon using (4.25) and (4.26), we have

$$\sum_{n=0}^{\infty}\Big[B_n^a + C_n^a\Big]J_0(\tau_n r) = 2i\beta\sum_{n=0}^{\infty} D_n^a \sin(s_n L)J_0(\tau_n r).$$

Multiplying both sides by $rJ_0(\tau_m r)$ and integrating from 0 to a , we obtain

$$\sum_{n=0}^{\infty}\Big[B_n^a + C_n^a\Big]\int_0^{\infty} J_0(\tau_n r)J_0(\tau_m r)rdr =$$
$$2i\beta\sum_{n=0}^{\infty} D_n^a \sin(s_n L)\int_0^{a} J_0(\tau_n r)J_0(\tau_m r)rdr.$$

On using orthogonality relation, we get

$$B_m^a + C_m^a = 2i\beta D_m^a \sin(s_m L). \tag{4.34}$$

By adding (4.33) and (4.34), we get

$$2B_m^a = \frac{2s_m}{\eta_m R_m} D_m^a \cos(s_m L) + 2i\beta D_m^a \sin(s_m L),$$

or

$$B_m^a = \Big[\frac{s_m}{\eta_m R_m}\cos(s_m L) + i\beta \sin(s_m L)\Big]D_m^a. \tag{4.35}$$

By subtracting (4.33) and (4.34), we get

$$2C_m^a = 2i\beta D_m^a \sin(s_m L) - \frac{2s_m}{\eta_m R_m} D_m^a \cos(s_m L),$$

or

$$C_m^a = \Big[i\beta \sin(s_m L) - \frac{s_m}{\eta_m R_m}\cos(s_m L)\Big]D_m^a. \tag{4.36}$$

The continuity condition of velocity at $z = -2L$ can be expressed as

$$\frac{\partial \phi_1^a}{\partial z} = W_1(r).$$

On using (4.23), we have

$$e^{ik(z+2L)}(ik) + \sum_{n=0}^{\infty} A_n^a J_0(\tau_n r)e^{-i\eta_n(z+2L)}(-i\eta_n) = \sum_{n=0}^{\infty} U_n J_0(\lambda_n r).$$

Multiplying both sides by $rJ_0(\tau_m r)$ and integrating from 0 to a , we obtain

$$ik\int_0^a J_0(\tau_m r)rdr + \sum_{n=0}^{\infty} A_n^a(-i\eta_n)\int_0^{\infty} J_0(\tau_n r)J_0(\tau_m r)rdr = \sum_{n=0}^{\infty} U_n \int_0^a J_0(\lambda_n r)J_0(\lambda_m r)rdr. \tag{4.37}$$

On using orthogonality relation, (4.37) becomes

$$A_m^a = \frac{k\delta_{mo}}{\eta_m} + \frac{i}{\eta_m R_m}\sum_{n=0}^{\infty} U_n R_{mn}. \tag{4.38}$$

The continuity condition of velocity is $\partial\phi_2^a/\partial z = W_1(r)$ at $z = -2L$.

Upon using (4.20) and (4.26), we have

$$\sum_{n=0}^{\infty}\left[B_n^a e^{-i\eta_n L}(i\eta_n) + C_n^a e^{i\eta_n L}(-i\eta_n)\right]J_0(\tau_n r) = \sum_{n=0}^{\infty} U_n J_0(\lambda_n r).$$

Multiplying both sides by $rJ_0(\tau_m r)$ and integrating from 0 to a, we get

$$\sum_{n=0}^{\infty} i\eta_n\left[B_n^a e^{-i\eta_n L} - C_n^a e^{i\eta_n L}\right]\int_0^a J_0(\tau_n r)J_0(\tau_m r)rdr = \sum_{n=0}^{\infty} U_m \int_0^a J_0(\lambda_n r)J_0(\tau_m r)rdr.$$

On using orthogonality relation, we get

$$B_m^a e^{-i\eta_m L} - C_m^a e^{i\eta_m L} = \frac{-i}{\eta_m R_m}\sum_{n=0}^{\infty} U_n R_{mn}. \tag{4.39}$$

Delany and Bazley [60] derived empirical formulae for the non-dimensional acoustic impedance Z_m^n and the propagation constant $\gamma = \alpha + i\beta$ based on experimental observation.

The strengths and shortcomings of the Delany and Bazley [60] formulation are

discussed in detail by Allard and Champoux [61] and Kirby and Cummings [62]. Their formulae, although unreliable for low frequencies, provide useful approximations and straightforward model which is suitable for mode-matching. The appropriate expressions are:

$$\frac{\alpha}{k} - = a_1 \xi^{a_3}. \tag{4.40}$$

The equation (4.40) describes how the attenuation of sound waves in the material depends on the frequency and material properties.

$$\frac{\beta}{k} = 1 + a_3 \xi^{a_4}. \tag{4.41}$$

The equation (4.41) describes how the phase of sound waves is modified as they propagate through the material.

$$\frac{r}{c\rho} = 1 + a_5 \xi^{a_6}. \tag{4.42}$$

The equation (4.42) describes how the resistive part of the acoustic impedance varies with frequency.

$$\frac{x}{c\rho} = -a_7 \xi^{a^8}. \tag{4.43}$$

The equation (4.43) describes how the reactive part of the acoustic impedance varies with frequency. The dimensionless frequency parameter ξ can be expressed as

$$\xi = \frac{\rho f}{\sigma}, \tag{4.44}$$

where ξ is dimensionless frequency parameter which often used in problems involving fluid dynamics, waves, or oscillations, particularly where surface tension plays a role, ρ represents the mass per unit volume of the fluid (It is a measure of resistance to acceleration) and the flow resistivity σ is given by:

$$\sigma = A_1 \rho_b^{A_2}. \tag{4.45}$$

In the equation (4.45) ρ_b is the bulk density for the porous material (realistic values for this lie in the region 100-180 kg/m^3), ρ is the density of air (1.2043 kg/m^3 at room temperature), f is frequency and the coefficients A_1, A_2 and $a_1 - a_8$ are found experimentally for a given porous material.

Kirby and Cummings [62], give the values for these coefficients for a range of commonly used porous materials.

Also Kirby and Cummings [62] investigated the acoustic properties of porous materials, particularly focusing on the propagation of sound waves within these materials and their interaction with boundary conditions. Their work aimed to improve the mathematical modeling of porous materials used in noise control applications by providing more accurate expressions for the effective density and bulk modulus of porous media.

They provided a modified version of the Delany and Bazley [60] empirical model, which describes the acoustic properties of fibrous absorbent materials. Their approach involved refining the expressions for characteristic impedance and wave number to improve accuracy for a broader range of frequencies and material properties, see Tables 4.1 and 4.2.

Material	**A-glass**	**E-glass**	**Basalt wool**	**Steel wool**
A_1	1.857	5.774	3.012	0.312
A_2	1.687	1.792	1.761	1.615

TABLE 4.1: Coefficients for steady flow resistivity for the porous materials

The Delany and Bazley [60] developed a set of widely used empirical expressions for predicting the acoustic properties of fibrous porous materials. These formulae provide approximations for the characteristic impedance and wave number of sound waves propagating in such materials based on their flow resistivity.

The Delany and Bazley [60] empirical formulae are still applicable but must be used in the form

$$\Gamma = \beta + i\alpha, \tag{4.46}$$

Material	**A-glass**	**E-glass**	**Basalt wool**	**Steel wool**	**Delany and Bazley [60]**
a_1	0.2251	0.2202	0.2178	0.1540	0.1890
a_2	-0.5827	-0.5850	-0.6051	-0.7093	-0.5950
a_3	0.1443	0.2010	0.1281	0.1328	0.0978
a_4	-0.7088	-0.5829	-0.6746	-0.5571	-0.7000
a_5	0.0924	0.0954	0.0599	0.0877	0.0571
a_6	-0.7177	-0.6687	-0.7664	-0.5557	-0.7540
a_7	0.1457	0.1689	0.1376	0.0876	0.0870
a_8	-0.5951	-0.5707	-0.6276	-0.7609	-0.7320

TABLE 4.2: Coefficients for bulk acoustic properties for the porous materials.

where α represents the imaginary part (indicating attenuation) and β represents the real part of the wave number (indicating phase speed), are given by (4.40) and (4.41).

4.4 Graphical Results of Problem 3

In this section, we present and analyze the graphical results for the real and imaginary parts of velocities in a porous medium adjacent to a soft wall.

The velocity components have been computed by solving the governing equations, and the solution is truncated to 15 terms to validate the matching conditions across different regions.

The results of matching conditions confirm that the velocity field is continuous across the porous region. The accuracy of the truncation method is validated as no significant deviation is observed. The continuity of the imaginary velocity components across the medium suggests a correct application of boundary conditions. The real and imaginary velocity components are in good agreement with theoretical predictions. Figures 4.9 - 4.12 confirm the validity of the solution in the presence of a soft wall at the back of the porous medium.

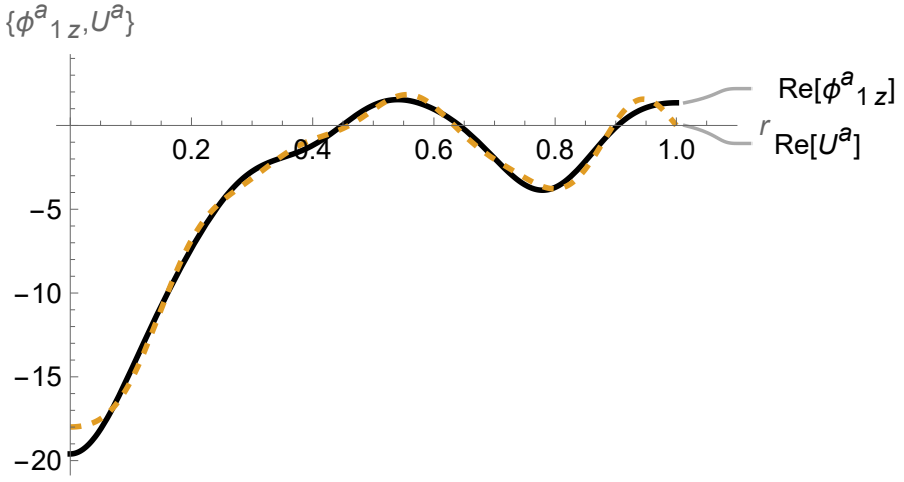

FIGURE 4.9: For soft wall: The real parts of velocities ϕ^a_{1z} and U^a against radius r at $z = -2L$ with 15 terms.

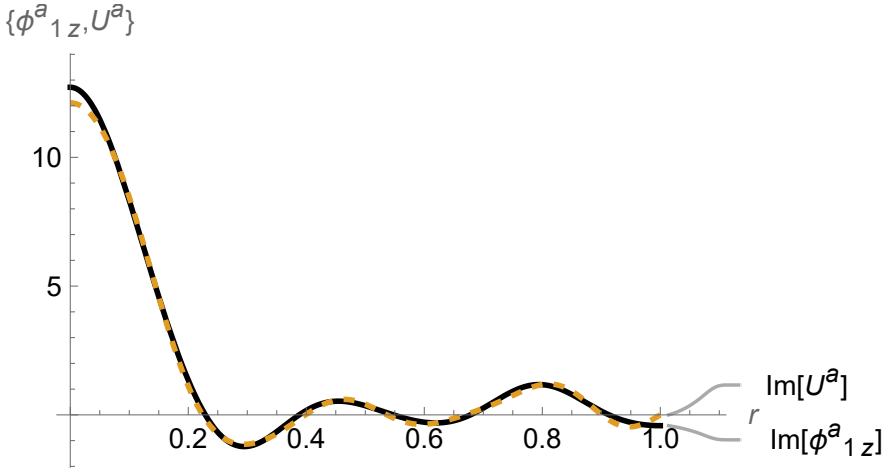

FIGURE 4.10: For soft wall: The imaginary parts of velocities ϕ^a_{1z} and U^a against radius r at $z = -2L$ with 15 terms.

Figure 4.13 is the density plot for anti-symmetric case that is for soft wall with $L = -0.3$.

The horizontal line represent z, ranging from -1 to -0.6 and the vertical line represent r, ranging from 0 to 1. The colored shown in Figure 4.13 represent the third dimension.

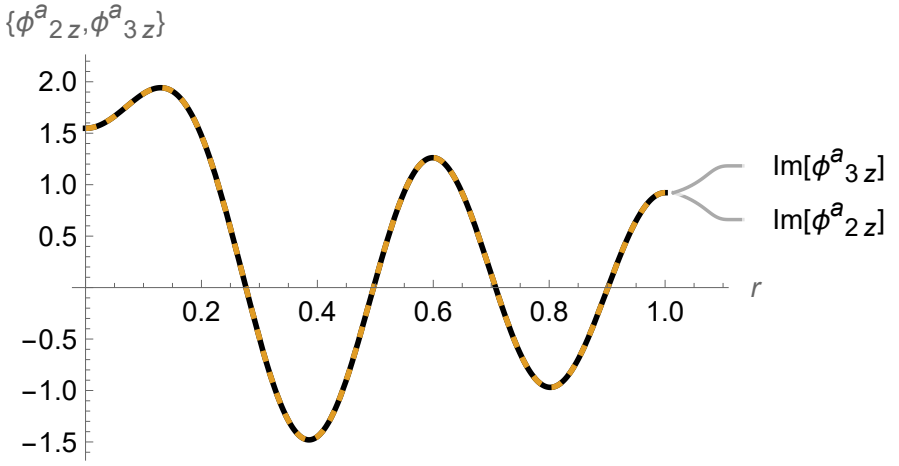

FIGURE 4.11: For soft wall: The real parts of velocities ϕ^a_{2z} and ϕ^a_{3z} against radius r at $z = -L$ with 15 terms.

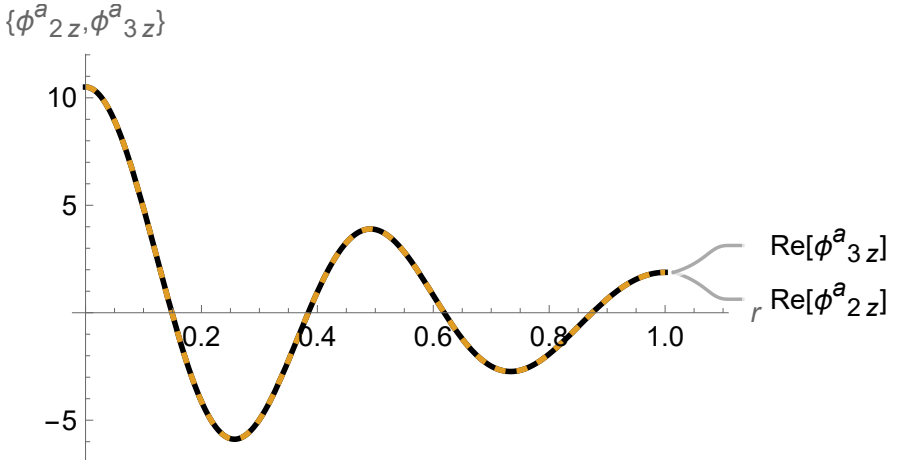

FIGURE 4.12: For soft wall: The imaginary parts of velocities ϕ^a_{2z} and ϕ^a_{3z} against radius r at $z = -L$ with 15 terms.

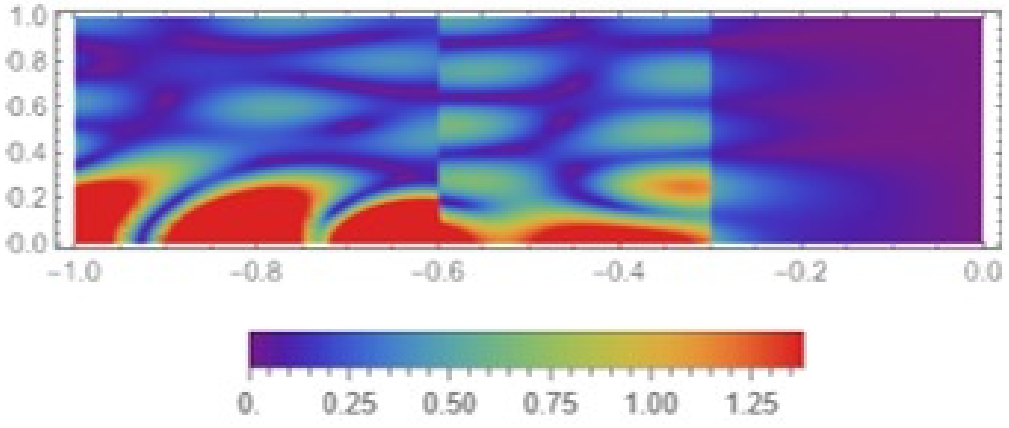

FIGURE 4.13: For anti-symmetric case: The density plots in whole domain $-1 < z < 0$ and $0 < r < a$ while $a = 1, L = -0.3$.

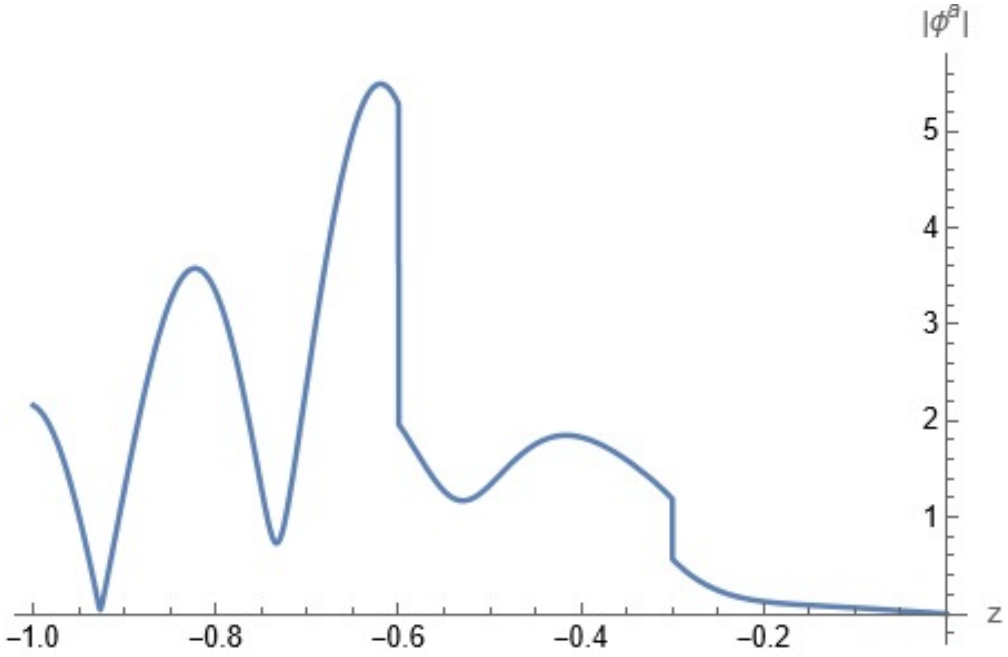

FIGURE 4.14: For anti-symmetric case: The graph of absolute value of ϕ^a against z while $-1 < z < 0$, where $L = -0.3, f = 1000, r = 0$.

4.5 Graphical Results and Discussion

The systems are solved using the MATHEMATICA software. Here, we compare 3D and 2D plots for both symmetric and anti-symmetric cases. In the first region of the density plot 4.6, the prominent red color signifies high modes of energy. As the energy transmits to the second region, the modes decrease in the air cavity region compared to the first region. In the third region of the density plot 4.6, the presence of red color indicates that the sound energy is not entirely filtered.

Figure 4.7 presents a 2D graph of the absolute value of ϕ^s against z, clearly illustrating that energy remains in the third region due to incomplete absorption caused by the rigid backing. For the anti-symmetric case, the first region of the density plot 4.13 displays a prominent red color, indicating high modes of energy. As the energy transmits to the second region, the modes decrease in the air cavity region compared to the first region. In the third region of the density plot 4.13, the absence of red color suggests that the sound energy is completely filtered.

Figure 4.14 is 2D graph of absolute value of ϕ^a against z, clearly demonstrating that energy is completely filtered in the third region. Comparing the density and

2D plots for both symmetric and anti-symmetric cases reveals that the soft wall absorbs sound energy more effectively than the rigid wall.

Chapter 5

Conclusion

This thesis focuses on the attenuation of sound waves using flexible structures backed by porous cavities, particularly in the context of low-frequency sound absorption.

The study employs mathematical modeling and numerical simulations to analyze the acoustic behavior of membrane-based waveguides and their interaction with porous materials. The key contributions of the thesis include:

- Mathematical Formulation: The study formulates the wave propagation problem using Helmholtz's equation, the membrane equation, and impedance boundary conditions. The mode-matching method is used to solve the boundary value problems, ensuring continuity of fields across interfaces.

- Orthogonality of Eigenfunctions: The eigenfunctions in the duct regions are shown to be orthogonal, which simplifies the solution of the boundary value problems.

- Numerical Results: The problem is solved numerically using MATHEMATICA, and the results demonstrate the effectiveness of the proposed approach in capturing the complex dynamics of the system. The study validates the truncated solution by showing the coincidence of velocity components at various frequencies.

- Flexible Structures with Porous Cavities: The study extends the analysis to include flexible structures backed by rigid and soft porous cavities, providing insights into the propagation and scattering of sound waves in such systems.

The study analyzes how membrane impedance and porous backing influence sound absorption characteristics. The rigid porous cavity shows stronger oscillations, indicating that waves are partially trapped and reflected while the soft porous cavity shows smoother variations, meaning it allows more wave energy to be absorbed rather than reflected. The thesis demonstrates that soft porous backing provides better low-frequency attenuation compared to rigid porous structures. The findings are relevant for noise control systems, particularly in industrial and urban environments where low-frequency sound absorption is crucial.

Bibliography

[1] P. Gorman, *Pythagoras: A Life*. Routledge, 1979.

[2] Aristotle, *On the Soul*. Clarendon Press, 350 BCE.

[3] G. Galilei, *Discourses and Mathematical Demonstrations Relating to Two New Sciences*. Macmillan, 1638.

[4] D. Bernoulli, "Recherches sur les vibrations des cordes sonores," *Mémoires de l'Académie de Berlin*, 1753.

[5] L. Euler, "Sur la vibration des cordes," *Nova Acta Eruditorum*, 1766.

[6] J. d'Alembert, "Recherches sur la courbe que forme une corde tendue mise en vibration," *Histoire de l'Académie Royale des Sciences et Belles-Lettres de Berlin*, 1747.

[7] R. Ford and M. McCormick, "Panel sound absorbers," *Journal of Sound and Vibration*, vol. 10, pp. 411–423, 1969. [Online]. Available: http://dx.doi.org/10.1016/0022-460X(69)90219-3

[8] M. Afzal, N. Ahmed, M. Safdar, and M. Umar, "On the modeling of sound sources in waveguides with structural variations and sound-absorbent materials," *Communication in Nonlinear Science and Numerical Simulation*, vol. 145, p. 108714, 2025.

[9] H. Bilal and M. Afzal, "Application of the matrix element method: A mode-matching approach for wave-bearing cavities in complex media," *Chaos, Solitons Fractals*, vol. 189, p. 115589, 2024.

[10] S. Rizvi and M. Afzal, "Electromagnetic wave scattering in plasma beam-driven waveguides under strong magnetic fields," *Communications in Theoretical Physics*, vol. 76, p. 115502, 2024.

[11] M. Afzal and T. Nawaz, "Trifurcated lined ducts: A comprehensive study on noise reduction strategies," *PLoS ONE*, vol. 19, no. 7, p. e0306115, 2024. [Online]. Available: https://doi.org/10.1371/journal.pone.0306115

[12] M. Afzal, T. Aziz, and H. M. S. Bahaidarah, "Dynamical behavior of fluid–structure interaction in ducts with rigid and flexible interfaces: Modeling and analysis," *Partial Differential Equations in Applied Mathematics*, vol. 11, p. 100789, 2024. [Online]. Available: https://doi.org/10.1016/j.padiff.2024.100789

[13] S. Shafique, M. A. Ahmad, and M. Afzal, "Optimizing the noise control in a two-layer conduit," *Physica Scripta*, vol. 99, p. 065227, 2024.

[14] M. Afzal, M. Safdar, and H. N. Alahmadi, "Analyzing the impact of flexible shells and sound absorbent lining on acoustic wave behavior in ducts," *Mathematical Methods in the Applied Science*, 2024. [Online]. Available: https://doi.org/10.1002/mma.10133

[15] S. Shafique, A. Ahmad, and M. Afzal, "Optimizing the noise control in a two-layer conduit," *Physica Scripta*, vol. 99, no. 6, p. 065227, 2024.

[16] S. Rizvi and M. Afzal, "Cold plasma-induced effects on electromagnetic wave scattering in waveguides: a mode-matching analysis," *Communications in Theoretical Physics*, vol. 76, no. 3, p. 035501, 2024.

[17] A. D. Alruwaili, M. Afzal, H. N. Alahmadi, and A. Wahab, "Wave scattering in cylindrical waveguides: Analyzing flexible shells and liner conditions," *Alexandria Engineering Journal*, vol. 91, pp. 610–619, 2024.

[18] A. D. Alruwaili, M. Afzal, M. Tanveer, and H. N. Alahmadi, "Analyzing monopole sources modeling with structural variations and material contrast: An analytical perspective," *Chaos, Solitons Fractals*, vol. 179, no. 1, p. 114434, 2024.

[19] M. Afzal, T. Nawaz, and R. Nawaz, "Scattering characteristics of planar trifurcated waveguide structure containing multiple discontinuities," *Waves in Random and Complex Media*, 2020.

[20] S. Shafique, M. Afzal, and R. Nawaz, "On the attenuation of fluid–structure coupled modes in a nonplanar waveguide," *Mathematics and Mechanics of Solids*, vol. 25, no. 10, pp. 1831–1850, 2020.

[21] M. Afzal and S. Shafique, "Attenuation analysis of flexural modes with absorbent lined flanges and different edge conditions," *Journal of the Acoustical Society of America*, vol. 148, no. 1, pp. 85–99, 2020.

[22] M. Afzal, J. U. Satti, and R. Nawaz, "Scattering characteristics of non-planar trifurcated waveguides," *Meccanica*, vol. 55, pp. 977–988, 2020.

[23] J. U. Satti, M. Afzal, and R. Nawaz, "Scattering analysis of a partitioned wave-bearing cavity containing different material properties," *Physica Scripta*, vol. 94, p. 115223, 2019.

[24] T. Nawaz, M. Afzal, and R. Nawaz, "The scattering analysis of trifurcated waveguide involving structural discontinuities," *Advances in Mechanical Engineering*, vol. 11, no. 7, pp. 1–10, 2019.

[25] H. Bilal and M. Afzal, "Acoustic wave scattering from a wave-bearing cavity in a rectangular waveguide," *Journal of the Acoustical Society of America*, vol. 144, p. 1681, 2018.

[26] A. Ullah, R. Nawaz, and M. Afzal, "Fluid-structure coupled wave scattering in a flexible duct at the junction of planar discontinuities," *Advances in Mechanical Engineering*, vol. 9, no. 7, pp. 1–11, 2017.

[27] J. B. Lawrie and M. Afzal, "Acoustic scattering in a waveguide with a height discontinuity bridged by a membrane: a tailored galerkin approach," *Journal of Engineering Mathematics*, vol. 105, no. 1, pp. 99–115, 2017.

[28] S. Shafique, M. Afzal, and R. Nawaz, "On mode matching analysis of fluid-structure coupled wave scattering between two flexible waveguides," *Canadian Journal of Physics*, vol. 95, no. 6, pp. 581–589, 2017.

[29] M. Afzal, R. Nawaz, and A. Ullah, "Attenuation of dissipative device involving coupled wave scattering," *Applied Mathematics and Computation*, vol. 290, no. 1, pp. 154–163, 2016.

[30] R. Nawaz, M. Afzal, and M. Ayub, "Acoustic propagation in two-dimensional waveguide for membrane bounded ducts," *Communications in Nonlinear Science and Numerical Simulation*, vol. 20, no. 2, pp. 421–433, 2015.

[31] H. Fuchs, *Applied Acoustics: Concepts, Absorbers, and Silencers for Acoustical Comfort and Noise Control*. Berlin: Springer, 2013. [Online]. Available: http://dx.doi.org/10.1007/978-3-642-29367-2

[32] H. Darcy, *Les fontaines publiques de la ville de Dijon*. Paris: Victor Dalmont, 1856.

[33] M. K. Hubbert, "The theory of ground-water motion," *Journal of Geology*, vol. 48, pp. 785–944, 1940.

[34] J. R. Philip and D. A. de Vries, "Moisture movement in porous materials under temperature gradients," *Transactions of the American Geophysical Union*, vol. 38, pp. 222–232, 1957.

[35] J. Bear and Y. Bachmat, *Introduction to Transport Phenomena in Porous Media*. Berlin: Springer, 1972.

[36] W. Fasold and E. Veres, *Schallschutz + Raumakustik in der Praxis*. Berlin: Bauwesen, 2003.

[37] C. Wang, J. Han, and L. Huang, "Optimization of a clamped plate silencer," *Journal of the Acoustical Society of America*, vol. 121, pp. 949–960, 2007. [Online]. Available: http://dx.doi.org/10.1121/1.2427126

[38] W. Frommhold, H. Fuchs, and S. Sheng, "Acoustic performance of membrane absorbers," *Journal of Sound and Vibration*, vol. 170, pp. 621–636, 1994. [Online]. Available: http://dx.doi.org/10.1006/jsvi.1994.1091

[39] Y. Lee, E. Lee, and C. Ng, "Sound absorption of a finite flexible microperforated panel backed by an air cavity," *Journal of Sound*

and Vibration, vol. 287, pp. 227–243, 2005. [Online]. Available: http://dx.doi.org/10.1016/j.jsv.2004.11.024

[40] R. Tayong, T. Dupont, and P. Leclaire, "On the variations of acoustic absorption peak with particle velocity in micro-perforated panels at high level of excitation," *Journal of the Acoustical Society of America*, vol. 127, pp. 2875–2882, 2010. [Online]. Available: http://dx.doi.org/10.1121/1.3372714

[41] K. Sakagami, M. Morimoto, and M. Yairi, "A note on the effect of vibration of a microperforated panel on its sound absorption characteristics," *Acoustical Science and Technology*, vol. 26, pp. 204–207, 2005. [Online]. Available: http://dx.doi.org/10.1250/ast.26.204

[42] M. Hiraizumi, K. Takahashi, T. Sone, and T. Nimura, "Study on the sound absorption by panel vibration—analysis in the model of circular panel with clamped boundary," *Journal of the Acoustical Society of Japan*, vol. 30, pp. 276–284, 1974.

[43] K. Sakagami and Others, "Analysis of an infinite elastic panel with an air-back cavity: Part i," *Journal of Sound and Vibration*, vol. 123, pp. 345–356, 2004.

[44] K. Sakagami, "Analysis of an infinite elastic panel with an air-back cavity: Part ii," *Journal of Sound and Vibration*, vol. 124, pp. 357–370, 2004.

[45] Y. Lee, H. Sun, and X. Guo, "Effects of the panel and helmholtz resonances on a micro-perforated absorber," *International Journal of Applied Mathematics and Mechanics*, vol. 4, pp. 49–54, 2005.

[46] J. Ford and A. McCormick, "Theoretical model for estimating sound absorption including mechanical vibration of a plate," *Journal of Acoustics and Vibrations*, vol. 47, pp. 125–134, 1983.

[47] M. Afzal and M. Safdar, "Mode-matching technique for analyzing scattering in elastic shell chambers: Applications in trifurcated waveguide systems," *Communication in Nonlinear Science and Numerical Simulation*, vol. 130, p. 107723, 2023.

[48] H. Bilal, M. U. Khan, and M. Afzal, "Silencing performance of the wave-bearing cavity with porous media," *Journal of Vibration and Control*, 2023. [Online]. Available: https://doi.org/10.1177/1077546323120938

[49] M. Afzal, M. O. Alkinidri, M. Safdar, and H. Bilal, "On the scattering of cylindrical elastic shell having trifurcation and structural variations at interfaces," *Chaos, Solitons Fractals*, vol. 175, p. 114033, 2023.

[50] M. Afzal, H. Bilal, N. Ahmed, and A. Wahab, "Acoustic scattering from a wave-bearing cavity with flexible inlet and outlet," *Mathematical Methods in the Applied Sciences*, 2023. [Online]. Available: https://doi.org/10.1002/mma.9633

[51] M. Safdar, N. Ahmed, M. Afzal, and A. Wahab, "Acoustic scattering in lined panel cavities with membrane interfaces," *Journal of the Acoustical Society of America*, vol. 154, pp. 1138–1151, 2023.

[52] M. Afzal, N. Akhtar, M. O. Alkinidri, and M. Shutaywi, "A mode-matching tailored-galerkin approach for higher order interface conditions and geometric variations," *Mathematics*, vol. 11, no. 3, p. 755, 2023.

[53] M. Afzal and H. Bilal, "Silencing performance analysis of a membrane cavity with different edge conditions," *Journal of Vibration and Control*, 2022. [Online]. Available: https://doi.org/10.1177/1077546322111870

[54] H. Bilal and M. Afzal, "Reflection and transmission of acoustic waves through the bridging membrane junctions," *Waves in Random and Complex Media*, 2022. [Online]. Available: https://doi.org/10.1080/17455030.2022.2051771

[55] Bilal and M. Afzal, "On the extension of the mode-matching procedure for modeling a wave-bearing cavity," *Mathematics and Mechanics of Solids*, vol. 27, no. 2, pp. 348–367, 2022.

[56] M. Afzal, J. U. Satti, R. Nawaz, and A. Wahab, "Scattering analysis of a partitioned membrane-bounded cavity with material contrast," *Journal of the Acoustical Society of America*, vol. 151, no. 1, pp. 31–44, 2022.

[57] T. Nawaz, M. Afzal, and A. Wahab, "Scattering analysis of a flexible trifurcated lined waveguide structure with step-discontinuities," *Physica Scripta*, vol. 96, no. 11, p. 115004, 2021.

[58] M. Afzal, S. Shafique, and A. Wahab, "Analysis of traveling waveform of flexible waveguides containing absorbent material along flanged junctions," *Communication in Nonlinear Science and Numerical Simulation*, vol. 97, p. 105737, 2021.

[59] M. Afzal and J. U. Satti, "The traveling wave formulation of a splitting chamber containing reactive components," *Archive of Applied Mechanics*, vol. 91, pp. 1959–1980, 2021.

[60] M. E. Delany and E. N. Bazley, "Acoustic properties of fibrous absorbent materials," *Applied Acoustics*, vol. 3, no. 2, pp. 105–116, 1970.

[61] J. F. Allard and Y. Champoux, "New empirical equations for sound propagation in rigid frame fibrous materials," *The Journal of the Acoustical Society of America*, vol. 91, pp. 3346–3353, 1992.

[62] R. Kirby and A. Cummings, "A note on the delany and bazley impedance model," *Applied Acoustics*, vol. 56, no. 3, pp. 271–278, 1998.